Hadron Phenomenology

PART 1. Hadronic Interactions at High Energy

C. Merino and Yu.M. Shabelski

Departamento de Física de Partículas and
Instituto Galego de Física de Altas Enerxías
Universidade de Santiago de Compostela
Galiza, Spain

November 2011

Master in Nuclear and Particle Physics and its Technological and Medical Applications

1 Introduction. Theoretical Situation

In subatomic world there is no unified theory, we have only some of its parts, see Bronstein cube (1937) presented in Fig. 1. The axis are mass M, velosity v and Plank constant h which has here the sence of inverse distance $1/R$.

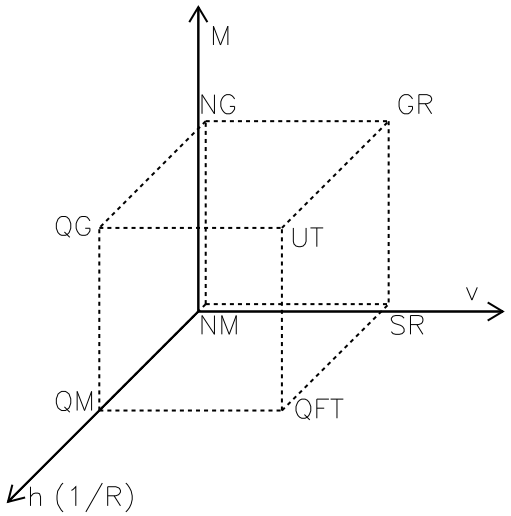

Figure 1: Bronstein cube: NM = Newton mechanics (+); SR = Special Relativity (+); QM = quantum mechanics (+); QFT = Quantum Field Theory (+/-); NG = Newton gravity (+); GM = General relativity (+); QG = Quantum Gravity (-); UT = Unified Theory of all interactions (-).

First four theories: Newton mechanics, special relativity, quantum mechanics, and Quantum Field Theory (QED, QCD,...) form **Standard Model**.

All physical theories are based on many experimental facts, these facts are especially important on the stage of formulation of a new theory. The Quantum Gravity is not exists as a real physical theory because there is no any experimental information about its effects.

In the present lectures we will consider mainly the Quantum Field Theory, today it can not be considered as a complete physical theory, so we present rather large quantity of experimental information - **phenomenology**.

2 Particles and Interactions

2.1 Sizes and Scales

All material objects in the Universe are builded from atoms.

In the present course we will consider the properties of the subatomic particles (elementary particles) and their interactions.

The scale of the significant sizes is given below:

1 m (meter)	$\rightarrow$	usual objects in our life
1 mm=10^{-3}m	$\rightarrow$	smallest objects which we can see by eye
1 μm=10^{-6}m (1 micron)		
1 nm=10^{-9}m (1 nanometer)	$\rightarrow$	size of atoms is about 0.1 nm
1 pm=10^{-12}m		
1 fm = 10^{-15}m (1 femtometer, 1 fermi)	$\rightarrow$	size of a nucleon

The probabilities of interactions of elementary particles are presented in terms of effective cross sections.

Cross Sections:

1 b (barn) $= 10^{-28}\text{m}^2$
1 mb $= 0.1$ fm^2
1 μb
1 nb
1 pb
1 fb

Masses and Energies ($c = 1$)

1 eV
1 KeV
1 MeV ($m_e = 0.511$ MeV)
1 GeV ($m_p = 0.94$ GeV)
1 TeV

In high energy elementary particle physics people usually work in "natural" units where $h = c = 1$.

In natural units length and time, that have same dimension, can be measured as inverse mass/energies:

$1 \text{ fm} \simeq 5 \text{ GeV}^{-1}$

$1 \text{ GeV}^{-2} \simeq 0.39 \text{ mb}$

$1 \text{ GeV}^{-1} \simeq 0.67 \cdot 10^{-24} \text{ seconds}$

2.2 Broad Classification of Sub-Nuclear Particles

All elementary particles can be divided in several groups:

HADRONS $\rightarrow$ have a size about 1 fm, (they have an internal quark-gluon structure)

LEPTONS AND GAUGE BOSONS $\rightarrow$ have no size, are considered as pointlike

Hadrons $\rightarrow$ Mesons, bosons, $q\bar{q}$)
Baryons, fermions, (qqq)

Leptons $\rightarrow$ $e^{\pm}, \mu^{\pm}, \tau^{\pm}$
ν_e, ν_μ, ν_τ

Gauge bosons $\rightarrow$ γ (Photon)
$Z^0, W^{\pm}$

2.3 Interactions of Sub-Nuclear Particles

There exist four types of interaction: **STRONG, ELECTROMAGNETIC, WEAK,** and **GRAVITATION**. All of them are produced via the exchange of a specific particle - gauge boson.

Electromagnetic and gravitation interactions are well-known in the usual world, and the strength both decrease with the distance as $1/R^2$. Such behaviour is connected with the zero mass of their gauge bosons - photon and graviton, respectively.

All material objects (including photons) participate of the gravitation interaction, and all particles with non-zero electrical charge participate in electromagnetical interaction.

The strong and weak interactions only exist in the subatomic world, because they exponentially decrease with distance.

The weak interaction is produced by the exchange of $W^{\pm}$ or Z bosons, $m_W = 80.4$ GeV, $m_Z = 91.2$ GeV.

Thus the typical distance of weak interaction is about 10^{-2} GeV^{-1}, i.e. 0.002 fm. As a rule we deal with weak interactions in the decay processes.

All leptons and hadrons participate in weak interactions. At very high energies the electromagnetic and weak interactions are unified in the framework of **Electroweak Theory**.

The strong interactions can be considered from two different points of view: as the interaction between hadrons via meson exchange, or as the interaction between quarks and gluons via gluon exchange.

2.4 An Example of Strong Interaction: One-Pion-Exchange

The meson exchange leads to the coupling of protons and neutrons in atomic nuclei. As the distance between nucleons in the nuclei is of the order of 1.2-1.5 fm, one can obtain (Yukawa, 1935) the mass of the lightest meson which obey this coupling, which turn out to be the pion ($m_\pi = 0.14$ GeV).

The meson exchange processes (mainly pion exchange) play an important role in the production of secondaries at not very high energies in so-called "soft" processes, i.e. in the processes with relatively small transverse momenta. For example, the diagrams presented in Fig. 2 describe the process of one-pion production in pp collision via Δ-resonance excitation.

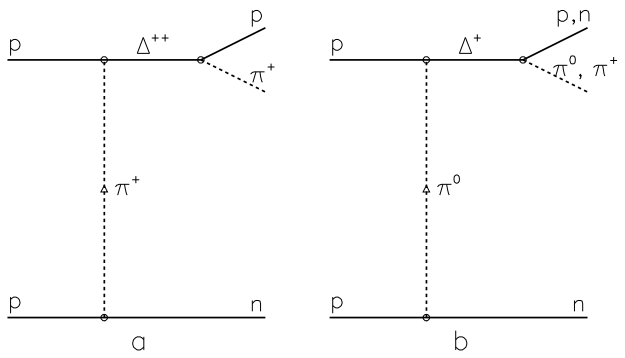

Figure 2: Pion production in pp collisions via $\Delta(1232)$ resonance excitation.

Due to the isospin invariance, all vertices in the diagrams of Fig. 2a and Fig. 2b are the same except for the corresponding Clebsch-Gordan coefficients.

2.5 The Quark-Gluon Structure of Hadrons

In the beginning of 1960's the number of discovered hadrons became very large (more than 200). Many physisicts tried to suggest relatively small more fundamental constituets, and, at the same time to obtain some classification of hadrons.

Gell-Mann and Zweig independently proposed in 1964 the SU(3) symmetry, where nucleons together with hyperons correspond to the octet representation of SU(3) group symmetry (p,n, $\Lambda, \Sigma^+, \Sigma^0, \Sigma^-, Xi^0, Xi^-$), light mesons ($\pi, K, \eta$ and η') correspond to the nonet representation, etc. The lowest representation of the SU(3) group is the triplet, and it was suggested that it correspond to some hypothetical particles carrying fractional electric charges, and called quarks (q).

noindent The most important property of quarks is that they cannot exist as free particle.

The quarks have a special quantum number, called **COLOUR**, which plays the role of their strong charge (coupling constant). There exist 3 colours, every quark has one of them and antiquarks have anticolours. The $q\bar{q}$ system with the same colour-anticolour is colourless (white) and corresponds to a meson.

The sum of all three colours is also white (remember the decomposition of white light by a glass prism), so all these qqq states corresponds to the baryons.

The quark-quark (or quark-antiquark) interaction proceeds via the exchange of a vector particle - gluon (g), which is bi-coloured. As gluons have colours they interact (contrary to the case of photons) with each other.

All interaction among quarks and gluons are decribed by special field theory - Quantum ChromoDynamics (QCD).

There exist four vertices of quark-gluon interactions shown in Fig. 3.

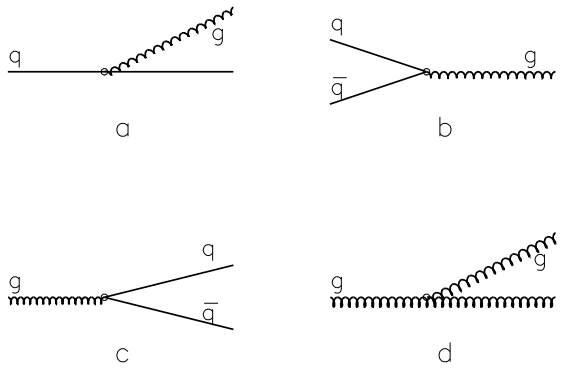

Figure 3: QCD vertices: gluon emission by quark (a); quark-antiquark annihilation into gluon (b); quark-antiquark pair production by gluon (c); gluon emission by gluon (d).

The strength of these interactions is determined by α_s - strong coupling constant.

Contrary to another theories (QED), α_s increases with the distance between two coloured particle, and it becomes infinitively large at distances of ~ 1 fm. This explains the phenomenon of **Quark Confinement**.

We cannot calculate anything when α_s becomes of the order of unity, so the microscopical theory of confinement does not yet exist.

At present we know 6 types of quarks, namely u, d, s, c, b, and t, which have names "up", "down", "strange", "charm", "beauty", and "top". The types of quarks are called "flavours". As quarks cannot be observed as free particles, their masses are not well-defined. However, the first three quarks are considered as light ones, whereas c, b, and t quarks are considered as heavy ones.

All quarks are fermions with spin 1/2. The quantum numbers of quarks are presented in Table 1:

flavour	charge	mass	other numbers
u	+2/3	1.5 to 4 MeV	Isospin = 1/2
d	-1/3	4 to 8 MeV	Isospin = 1/2
s	-1/3	80 to 130 MeV	Strangeness = -1
c	+2/3	1.15 to 1.35 GeV	Charm = +1
b	-1/3	4.1 to 4.9 GeV	Bottom = -1
t	+2/3	170 to 185 GeV	Top = +1

Table 1. Quantum numbers of quarks.

When we consider hadrons as bound systems of quarks, two approaches can be used.

In the case of hard interactions with large transfer momenta, hadron consist of valence quarks which masses are presented in Table 1, as well as of gluons and of quark-antiquark pairs which are produced radiatively by gluons (see Fig. 3c). The quarks from these pairs are called sea-quarks.

When considering hadron systematics and soft hadron interaction, gluons and sea pair can be included in the content of an effective object called constituent quark. So in this cases, we can consider mesons and baryons as $\bar{q}q$ and qqq systems, respectively.

3 Relativistic kinematics, $2 \to 2$ Scattering Amplitude, and Cross Sections

3.1 Mandelstam Variables

We will consider mainly the particle interactions at high energies. In this case energy E and vector momentum $\mathbf{p}$ of a particle with mass m and velocity v are given by

$$E = \frac{mc^2}{\sqrt{1 - \frac{v^2}{c^2}}} \ , \quad \mathbf{p} = \frac{m\mathbf{v}}{\sqrt{1 - \frac{v^2}{c^2}}} \ . \tag{3.1}$$

The energies and momenta of a particle in different frames can be calculated using the Lorentz transformations. However such calculations becomes more simple if one use 4-dimential vectors and relativistic invariants. The energy E and 3-momentum $\mathbf{p}$ of a particle of mass m form a 4-vector $p = (E, \mathbf{p})$, whose square $p^2 \equiv E^2 - |\mathbf{p}|^{\mathbf{2}} = \mathbf{m^2}$ is relativistic invariant. The velocity of the particle is $\beta = v/c = |\mathbf{p}|/\mathbf{E}$.

The simplest situation is the $2 \to 2$ particles interaction, it can be elastic (say, $pp \to pp$) or inelastic (say, $\pi^- p \to K^0 \Lambda$) collision, see Fig. 4.

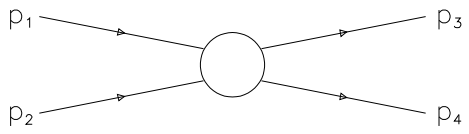

Figure 4: Two-particle final state in collision of two hadrons with momenta p_1 and p_2.

Let us consider the case when two particles 3 and 4 are produced in the collision of incident particles 1 and 2

$$1 + 2 \to 3 + 4 \ , \tag{3.2}$$

and let p_1, p_2, p_3, p_4 and m_1, m_2, m_3, m_4 be their 4-dimential moments and masses, respectively. So we have

$$\begin{aligned} p_1 + p_2 &= p_3 + p_4 \\ p_1^2 = m_1^2,\ p_2^2 = m_2^2,\ p_3^2 &= m_3^2,\ p_4^2 = m_4^2 \\ (p_1 + p_2 - p_3)^2 &= p_4^2 = m_4^2 \end{aligned} \tag{3.3}$$

Let us introduce the Lorentz-invariant **Mandelstam variables** which are defined by

$$\begin{aligned} s &= (p_1 + p_2)^2 = (p_3 + p_4)^2 \\ t &= (p_1 - p_3)^2 = (p_2 - p_4)^2 \\ u &= (p_1 - p_4)^2 = (p_2 - p_3)^2 \ , \end{aligned} \tag{3.4}$$

and they satisfy

$$s + t + u = m_1^2 + m_2^2 + m_3^2 + m_4^2 \ , \tag{3.5}$$

so only two variables are independent. Usually s and t are chosen as the two independent variables for $2 \to 2$ process.

The variable s has a physical sence of energy. In lab. frame

$$s = p_1^2 + p_2^2 + 2p_1 \cdot p_2 = m_1^2 + m_2^2 + 2m_2 E_{1lab.} \ , \tag{3.6}$$

because $\mathbf{p}_2 = 0$ and $p_1 \cdot p_2 = m_2 E_{1lab.}$.

In c.m. frame by definition $\mathbf{p}_2 = -\mathbf{p}_1$, so $p_1 \cdot p_2 = E_1 E_2 + |\mathbf{p}|^2$ and

$$s = (E_{1cm} + E_{2cm})^2 \ . \tag{3.7}$$

In many cases it is interesting to know the c.m. energies of final particles 3 and 4 for given value of s. They are given by expressions

$$E_{3cm} = \frac{s + m_3^2 - m_4^2}{2\sqrt{s}} \ , \ E_{4cm} = \frac{s + m_4^2 - m_3^2}{2\sqrt{s}} \ . \tag{3.8}$$

The variables t and u, Eq. (3.4) have a physical sence of transfer momenta.

In the important case of elastic scattering when particles 1 and 3 as well as 2 and 4 coinside we have in c.m. frame

$$t = -2|\mathbf{p}|^2(1 - cos(\theta) = -4|\mathbf{p}|^2 sin^2(\theta/2) \ . \tag{3.9}$$

3.2 S-matrix and scattering amplitude

Here we will consider the formalism of so-called S-matrix. We will see that using the very general its properties, such as unitarity, analiticity, conservation laws, etc., allow one to obtain very important information about interactions of elementary particles.

Let us consider a sample of physical states and possible transitions of state Φ_i into state Φ_f. It is equal to the modulo squared of the correspondent matrix element of S-matrix:

$$S_{fi} = \langle \Phi_f^+(t = +\infty) | \hat{S}(+\infty, -\infty) | \Phi_i(t = -\infty) \rangle \ . \tag{3.10}$$

The S-matrix elements themselves are evaluated between asymptotic states at times $t = \pm\infty$ (the initial state a long time before the interaction commences and the final state a long time afterwards).

If the interaction is absent, the state of the system cannot be changed, that corresponds to the unit S-matrix $I = \delta_{fi}$. Generally

$$S_{fi} = \delta_{fi} + iT_{fi} \tag{3.11}$$

The transitions between states i and f are possible if $T_{fi} \neq 0$ and the matrix elements T_{fi} determine the transition amplitude $A(i \to f)$. This amplitude is a Lorents-invariant scalar determined as

$$T_{fi} = (2\pi)^4 \delta^{(4)}(\sum p_i - \sum p_f) A(i \to f) \; . \tag{3.12}$$

The Lorentz invariant amplitude $A(i \to f)$ is called a **scattering amplitude**, it depends only on Lorentz invariant scalars.

3.3 Crossing and physical regions

The scattering amplitudes are the analitical functions of their variables. It means that the amplitude $A(p_1, p_2, p_3, p_4)$ has physical sence at arbitrary values of p_1, p_2, p_3, p_4. The important point here is that the incoming particle with negative value of 4-momentum (in the sense that if $p_1 + p_2 = p_3 + p_4$, $p_3 + p_4 - p_1 - p_2 = 0$) becomes the outgoing antiparticle with positive 4-momentum, and vice versa.

For example, let us consider the elastic proton-neutron scattering. It means that the incident and final state proton has momenta p_1 and p_3, whereas the incident and final state neutron has momenta p_2 and p_4 and the scattering amplitude for the process $1+2 \to 3+4$ is $A_{1+2\to3+4}(p_1, p_2, p_3, p_4)$.

The crossing assumption means that the same analitical function should describe the processes $1+\bar{3} \to \bar{2}+4$ and $1+\bar{4} \to \bar{2}+3$. So, we have

$$\begin{array}{llllll} \text{s-channel,} & p+n \to p+n, & s>0 & t<0 & u<0 \\ \text{t-channel,} & p+\bar{p} \to n+\bar{n}, & t>0 & s<0 & u<0 \\ \text{u-channel,} & p+\bar{n} \to p+\bar{n}, & u>0 & t<0 & s<0 \end{array}$$

The values of variables s, t, u in these three cases are not overlapping. The situation can be shown in the so-called Mandelstam plane with triangle coordinates shown in Fig. 5.

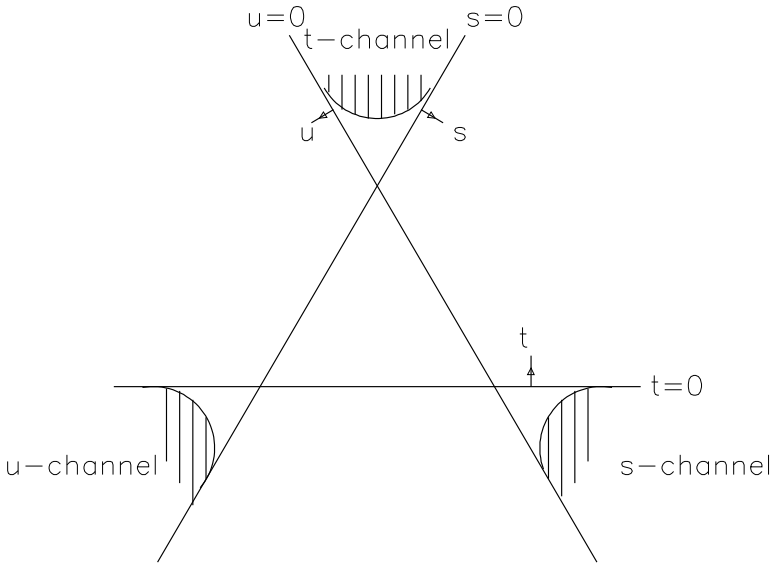

Figure 5: Mandelstam plane for elastic scattering $1 + 2 \to 3 + 4$.

The shape of curves in Fig. 5 that show the boundaries of s-, t- and u-channels depend on the masses of initial as well as final particles.

3.4 Probabilities of transitions and decays

The probability of transition of initial state i into final state f $(i \neq f)$ during a unit of time t is equal to

$$\tilde{w}_{i\to f} = \frac{1}{t}|T_{fi}|^2 = \frac{1}{t}(2\pi)^8[\delta(\Sigma\, p_i - \Sigma\, p_f)]^2|A(i \to f)|^2 \tag{3.13}$$

Here we have the square of δ-function. The δ-function is an operator determined as

$$\int f(x)\delta(x-a)dx = f(a)\ . \tag{3.14}$$

One δ-function in Eq. (3.13) can be represent as

$$\delta^4(\Sigma\, p_i - \Sigma\, p_f) = \frac{1}{(2\pi)^4}\int d^4x e^{(\Sigma\, p_i - \Sigma\, p_f)x}\ . \tag{3.15}$$

The probability of transition

$$\tilde{w}_{i\to f} = (2\pi)^4\,\delta(\Sigma\, p_i - \Sigma\, p_f)\,|A(i\to f)|^2\,V\ . \quad (3.16)$$

To account for that several final states are possible the probability of transition $\tilde{w}_{i\to f}$ should be multiplied by the number of final states in the volume V, that is equal to

$$\Phi = \prod_{k=1}^{n} \frac{V d^3 p_k}{(2\pi)^3}\ , \quad (3.17)$$

where n is the number of particles in the final state and p_k is the 3-dimential momentum of k-th particle and be divided by

$$N = \prod_{i=1}^{l} 2E_i V \cdot \prod_{k=1}^{n} 2E_k V \quad (3.18)$$

that is connected with normalization of the initial and final wave functions.

As a result, we obtain the normalized probability of transition in the form

$$dw_{i\to f} = \left[\prod_{i=1}^{l} 2E_i V\right]^{-1} V\,|A(i\to f)|^2\,d\tau_n\ , \quad (3.19)$$

where

$$d\tau_n = (2\pi)^4\,\delta(\Sigma\,p_i - \Sigma\,p_f)\ \prod_{k=1}^{n}\frac{d^3p_k}{((2\pi)^3 2E_k} \quad (3.20)$$

is the n**-particle phase space**. In Lorentz-invariant form it can be written as

$$\frac{d^3p_k}{(2\pi)^3 2E_k} = \frac{d^4p_k}{(2\pi)^3}\delta(p_k^2 - m_k^2)\ . \quad (3.21)$$

In the case of decay of a particle with mass m into several (n) ones in the rest frame, $E_{i=1} = m$,

$$dw_{i\to f} = \frac{1}{2m}|A(i\to f)|^2\,d\tau_n\ . \quad (3.22)$$

3.5 Differential cross sections

In the case of collision of two particles with vector momenta p_a and p_b and energies E_a and E_b. The most important physical value is the **cross section** that shows the effective range of particle interaction. Cross section can be obtained by dividing the probability dw by the flow density j of incident particles

$$d\sigma_{i\to f} = dw_{i\to f}/j \ , \tag{3.23}$$

where

$$j = \frac{I}{VE_aE_b} \ , \tag{3.24}$$

that results in

$$d\sigma = \frac{|A(i \to f)|^2}{4I} d\tau_n \ , \tag{3.25}$$

where

$$I = \sqrt{(p_a p_b)^2 - m_a^2 m_b^2} \tag{3.26}$$

In the case when only two particles exist in the final state we obtain in c.m. frame

$$d\sigma = \frac{1}{64\pi^2}\,|A(i \to f)|^2 \frac{|p|}{|p_0|\,E_0^2}\,d\Omega\ . \qquad (3.27)$$

where $|p_0|$ and E_0 are the the modulo of the momentum and energy in the initial state and $|p|$ is the modulo of the momentum in final state.

In the important case of elastic scattering and azimuthal symmetry $d\Omega = 2\pi dcos(\theta)$ $|p_0| = |p|$, $d\Omega = 2\pi dcos(\theta)$, $dt = 2|p|^2 dcos(\theta)$ and we obtain

$$\frac{d\sigma}{dt} = \frac{1}{64\pi^2|p|^2 s}\,|A_{el}|^2 = \frac{1}{64\pi^2|p_{a(lab)}|^2 m_b^2}|A_{el}|^2\ . \qquad (3.28)$$

Sometimes it is suitable to define the scattering anplitude by another way, as

$$f_{i\to f} = \frac{A_{i\to f}}{8\pi\sqrt{s}} \ , \quad \frac{d\sigma(ab \to ab)}{d\Omega_{c.m.}} = |f_{ab\to ab}|^2 \ . \quad (3.29)$$

or as

$$M_{i\to f} = \frac{A_{i\to f}}{16\pi p_0\sqrt{s}} \ , \quad \frac{d\sigma}{dt} = 4\pi|M_{ab\to ab}|^2 \quad (3.30)$$

The integral of considered differential cross section determines the total cross section of the considered process

$$\sigma(a + b \to 1 + 2) \ . \quad (3.31)$$

The sum of all possible channels corresponds to the **total cross section** of ab interaction.

4 Unitarity

4.1 Unitarity of S-matrix

The very important property of S-matrix is its unitarity:

$$S^+S = 1 \ , \quad (S^+S)_{fi} = \sum_n S^*_{nf} S_{ni} = \delta_{fi} \ . \tag{4.1}$$

Here we sum over all channels n and integrate over all variables of the intermediate states.

In the case of only diagonal transitions ($i = f$)

$$\sum_n |S_{ni}|^2 = 1 \ , \tag{4.2}$$

it means that the sum of the probabilities of all possible transitions is equal to unity.

Eq. (4.1) can be written as

$$(S^+S)_{fi} = \sum_n (\delta_{fn} - iT^+_{fn})(\delta_{ni} + iT_{ni}) = \delta_{fi} \ , \tag{4.3}$$

i.e.

$$T_{fi} - T^*_{if} = \sum_n iT^*_{nf} T_{ni} \ . \tag{4.4}$$

For the amplitudes A we obtain

$$A(i \to f) - A^*(i \to f) = i(2\pi)^4 \sum_n \delta(\sum p_n - \sum p_f) A(i \to n) \cdot A \tag{4.5}$$

that is the **unitarity condition fo the scattering amplitude**.

In the most important case of elastic scattering $i = f$ and we have

$$2ImA_{el} = (2\pi)^4 \sum_n \delta(\sum p_n - \sum p_f) |A(i \to n)|^2 \,, \tag{4.6}$$

where the imaginary part of elastic scattering amplitude $ImA(i \to i)$ is expressed via the sum af all possible intermediate states n. So, we have

$$\begin{aligned} ImA_{el}(s,t) &= \frac{1}{2} \sum_n \int |A(i \to n)|^2 d\tau_n \\ &= \frac{1}{2} \sum_n \Delta A^{(n)}(s,t) = \frac{1}{2} \Delta A(s,t) \,, \end{aligned} \tag{4.7}$$

that is non-zero only at $\sqrt{s} \geq \sqrt{s_n}$, where s_n is the threshold energy for the correspondent channel.

New contributions to **absorptive part** $\Delta A^{(n)}$ of elastic scattering amplitude will appear with increaase of energy, when new inelastic channels will appear.

4.2 Optical Theorem

From unitarity condition we obtain

$$ImA_{i\to i}(q=0) = 2p_0\sqrt{s}\,\Sigma\,\sigma_n = 2p_0\sqrt{s}\,\sigma^{tot}\ . \quad (4.8)$$

that is called the **optical theorem**.

As an analogy with classical optic, imaginary part of elastic scattering amplitude determines the absorption of icident particle, whereas the real part determines its refraction.

4.3 An example: $K_L^0 \to \mu^+\mu^-$ decay

Let us consider the probability of rare decay $K_L^0 \to \mu^+\mu^-$ that was considered as a problem in early 70's. During some time this decay was not discovered.

there were theoretical reasons to think that the main contribution to the discussed decay comes from the diagram shown in Fig. 6, i.e via $\gamma\gamma$ intermediate state.

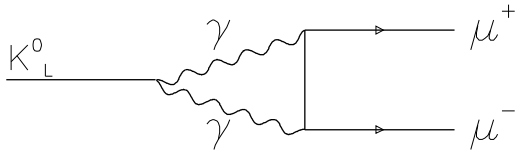

Figure 6: $K_L^0 \to \mu^+\mu^-$ decay via $\gamma\gamma$ intermediate state.

From the unitarity condition the imaginary part of the considered amplitude is determined by

$$ImA(K_L^0 \to \mu^+\mu^-) = \int A^*(\mu^+\mu^- \to \gamma\gamma)A((K_L^0 \to \gamma\gamma)d\tau_{\gamma\gamma} \tag{4.9}$$

The amplitude in the right-hand side are known, the first one from QED and the second one from the known decay $K_L^0 \to \gamma\gamma$ that allows one to calculate the low boundary for $K_L^0 \to \mu^+\mu^-$ decay probability.

4.4 n-particle phase space and behaviour of cross sections near the threshold

The phase space of n secondary particles can be calculated by using the multiplicative expression which allow one to present $d\tau_n$ as the product of τ_{n_1} and $\tau_{n_2=n-n_1}$.

$$d\tau_n = d\tau_{n-1}(W_1) d\tau_2(\sqrt{s}, W_1, m_n^2) \frac{dW_1^2}{(2\pi)} \ , \qquad (4.10)$$

where W_1 is is the c.m. energy of $n-1$ particles.

For example, in the case of three particle in the final state

$$d\tau_3(\sqrt{s}) = d\tau_2(W_1, m_1^2, m_2^2)\, d\tau_2(\sqrt{s}, W_1, m_3^2)\, \frac{dW_1^2}{(2\pi)} \ . \qquad (4.11)$$

Near the threshold of n particle production, s_n, all of them are non-relativistic ones. In this case one can obtain

$$\tau_n(s) \sim (s - s_n)^{\frac{3n-5}{2}} \ . \tag{4.12}$$

The amplitude should not have a strong dependence on these variables in rather small energy region (some special reasons are needed for this) So the energy dependence of particle production cross section near the threshold should be determined by non-relativistic phase space.

In particular, for two-particle final state we have

$$\sigma_2(s) \sim (s - s_n)^{1/2} \ , \tag{4.13}$$

for three-particle final state

$$\sigma_3(s) \sim (s - s_n)^2 \ , \tag{4.14}$$

and for four-particle final state

$$\sigma_4(s) \sim (s - s_n)^{7/2} \ . \tag{4.15}$$

The comparison of these prediction for the reactions with three-particle final state and four-particle final state are presented in Fig. 8.

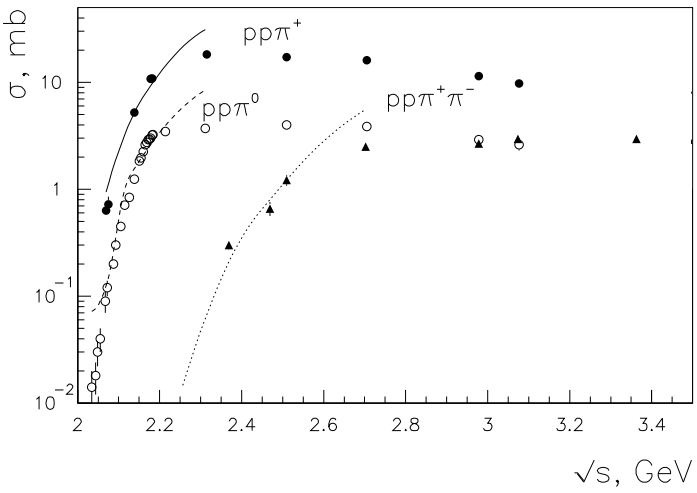

Figure 7: Energy dependence of reactions $pp \to pn\pi^+$ (black points), $pp \to pp\pi^0$ (open points), and $pp \to pp\pi^+\pi^-$ (triangles) near threshold. The curves represent Eq. (4.13) and Eq. (4.14) energy dependences normalized to one experimental point for every reaction.

The non-relativistic expressions for phase space reasonably describe the energy dependences of the considered reactions near thresholds. With increase of energy the energy dependences of reaction amplitudes become important and the energy dependences of reaction cross sections changes.

4.5 Froissart theorem

In 1961 M. Froissart obtained the bound fo the increase of total cross section with the energy.

$$\sigma^{tot}(s) \leq C \ln^2 s \ , s \to \infty \ . \qquad (4.16)$$

The idea of this boundary comes from the Yukawa potential for strong interactions, the probability of interactio at large distance r, $P(r) = P_0 e^{-br}$. The total inelastic cross section can not be larger that the geometrical one π/b^2 and the corrections to this estimation can not be more strong than the logarithmical ones.

The detaile proof of boundary Eq. (62) is based on the partial vawes (i.e. orbital momentum) expansion and on dispersion relations (see next Section) and can be found in the original paper

M.Froissart. Phys.Rev. **123** , 1053 (1961).

5 Analiticity and dispersion relations

5.1 Structure of singularities for high energy particle collision

All physical amplitudes are assumed to be the analutycal functions of their variables.

At energies below the elastic treshold, i.e. at $s < (m_a + m_b)^2$ the elastic scattering amplitude $a + b \to a + b$ usually is pure real

At $s > (m_a + m_b)^2$ the values $A(s + i\varepsilon)$ and $A(s - i\varepsilon)$ become different at $\varepsilon \to o$. It means that there exists a cut in the real axix of complex s-plane which start at the point $s = s_2 = (m_a + m_b)^2$ and goes to infinity, as it is shown in Fig. 8.

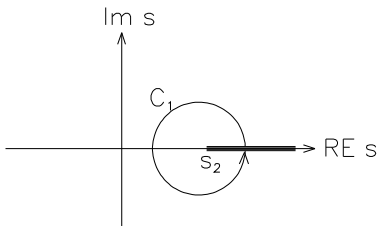

Figure 8: Elastic scattering amplitude $1+2 \to 1+2$ together with its first two-particles cut in the complex s-plane.

The physical amplitude is determined on the up border of the cut, i.e.$A(s+i\varepsilon)$ and this part of plane is called as **physical sheet**.

At higher energy new branching points s_3 and the cuts appeaer. The discontinuity of the lastic scattering amplitude is the difference of its values on the up and dpown borders of the cut

$$\Delta A(s) = A(s+i\varepsilon) - A(s-i\varepsilon)\ , \qquad (5.1)$$

that coinside with the absorptive part of the amplitude.

The examples of simple mathematical functions that have similar analitical properties are the functions

$$f_1(s) = a_1 + b_1(s_n - s)^{m+1/2} \qquad (5.2)$$

and

$$f_2(s) = a_2 + b_2(s_n - s)^m \ln(s_n - s)\ . \qquad (5.3)$$

The discontinuity $\Delta f_1(s)$ and $\Delta f_2(s)$ coinside with the cuts connected with even number $n = 2m$ of and odd number $n = 2m+1$ of produced particles, respectively.

For the determination of the scattering amplitude $A(s)$ one should to present all its cuts in the complex s-plane from $s = s_n$ until infinity, as it is shown in Fig. 9.

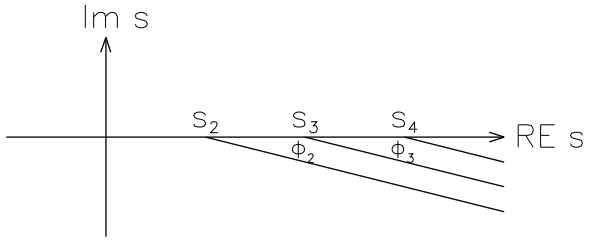

Figure 9: Elastic scattering amplitude $a + b \to a + b$ with its two-particle, three-particle and four-particle branching point that correspondent to particle production in the intermediate state together with the corresponding cuts in the complex s-plane. Really all angles $\phi_i \to 0$.

For fixed value of variable $t = t_0$ the variable u that corresponds to the u-channel reaction $1 + \overline{4} \to \overline{2} + 3$ changed in dependence of s value, as $u = \Sigma\, m_i^2 - s - t$. This point is also the branching point of the amplitude $A(s)$, and the correspondent cut exists in the real axes of s in the negative direction, until $s = -\infty$.

Usually there exists the region where the scattering amplitude is real and $A^*(s) = A(s^*)$. The physical amplitude is determined upper the right-hand-side cut and below the left-hand-side cut, i.e.

$$A(s) = A(s + i\epsilon) \; , A(u) = A(u + i\epsilon) = A(s - i\epsilon) \; . \tag{5.4}$$

the discontinuity on the right-hand cut

$$\Delta A_1(s, t_0) = \sum_n \Delta A^{(n)}(s, t_0) = ImA_{a+b\to a+b}((s+i\epsilon, t_0) \tag{5.5}$$

and the discontinuity on the left-hand cut

$$\Delta A_2(u, t_0) = \sum_n \Delta A^{(n)}(u, t_0) = ImA_{a+\bar{b}\to a+\bar{b}}(s-i\epsilon, t_0) \; . \tag{5.6}$$

5.2 Poles of the scattering amplitude and dispersion relation at fixed t

The scattering amplitude at the point $s + i\delta$ can be written as the Cauchy integral over an arbitrary conteur around this point on the physical sheet

$$A(s + i\delta, t_0) = \frac{1}{2\pi i} \oint \frac{A(s')}{s' - (s + i\delta)} \, ds' \, . \qquad (5.7)$$

If the only singularities of the scattering amplitude on the physical sheet are the cuts and branching points and the cuts are not overlapped, one can deform the conteur and obtain it as is shown in Fig. 10.

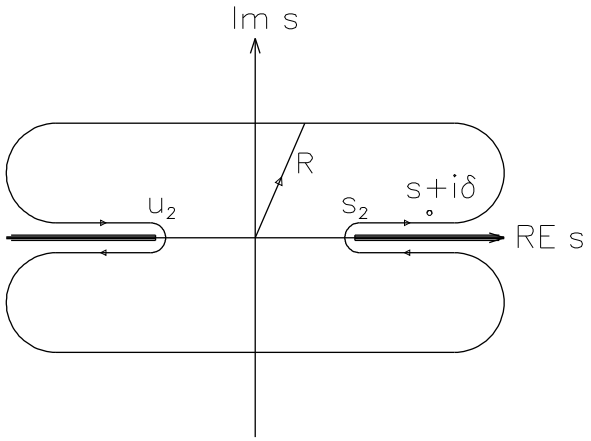

Figure 10: Conteur integral which determines the elastic scattering amplitude in the point $s + i\delta$.

If the amplitude $A(s)$ decrease at $s \to \infty$ faster than $1/(\ln s)^2$, the first integral over contout C_R is negligible at $R \to \infty$ and we obtain

$$A(s, t = t_0) = \frac{1}{\pi} \int_{s_2}^{\infty} \frac{\Delta A_1(s', t_0)}{s' - s - i\delta} ds'. + \qquad (5.8)$$
$$+ \frac{1}{\pi} \int_{u_2}^{\infty} \frac{\Delta A_2(u', t_0)}{u' - u + i\delta} du' \quad \delta \to 0 \; .$$

In many cases in the system ab (or in the system $a\bar{b}$) there exists bound states with $m^2 < s_2$, or $m^2 < u_2$. The simplest example is a pion in the case of $N\bar{N}$ scattering.

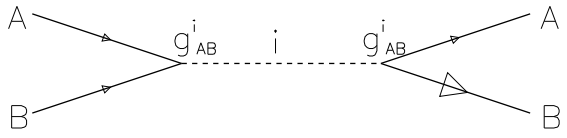

Figure 11: Elastic scattering amplitude $a + b \to a + b$ via s-channel pole.

For the case of only one pole, see Fig. 11, we obtain

$$\Delta A_1(s, t_0) = \pi |g^i_{AB}|^2 \delta(s - s_i) \qquad (5.9)$$

with $s_i = m_i^2$ that should be accounted for.

Accounting for both the poles in s-channel and in u-channel we can write the final expression as follows

$$A(s,t_0) = \sum_i \frac{a_i}{(s_i - s)} + \sum_j \frac{a_j}{(u_j - u)} + \tag{5.10}$$
$$+ \frac{1}{\pi}\int_{s_2}^{\infty} \frac{\Delta A_1(s',t_0)}{s' - s - i\delta} ds'. + \frac{1}{\pi}\int_{u_2}^{\infty} \frac{\Delta A_2(u',t_0)}{u' - u + i\delta} du' \ .$$

This expression is known as the **dispersion relation** for the elastic scattering amplitude at fixed $t = t_0$.

Here it is assumed that on the physical sheet there exist only poles and cuts and all another singularities of the elastic scattering amplitude are placed on unphysical sheets.

5.3 Real part of the elastic scattering amplitude

In the operator sence

$$\frac{1}{s' - s \mp i\epsilon} = \frac{1}{s' - s} \pm i\pi\delta(s' - s) \,, \qquad (5.11)$$

so we can write the **real part of the amplitude** as

$$\begin{aligned} ReA(s,t_0) \;=\; & \sum_i \frac{a_i}{(s_i - s)} + \sum_j \frac{a_j}{(u_j - u)} + \qquad (5.1 \\ & + \; P\frac{1}{\pi}\int_{s_2}^{\infty} \frac{\Delta A_1(s',t_0)}{s' - s} ds' + P\frac{1}{\pi}\int_{u_2}^{\infty} \frac{\Delta A_2(u',t_0)}{u' - u} du \end{aligned}$$

If the elastic scattering amplitude $A(s,t_0)$ decrease with s slower than $1/\ln^2 s$, one can write the Couchet integral Eq. (5.10) for the quantity

$$A^{(1)}(s) = \frac{A(s) - A(s_0)}{s - s_0} \,, \qquad (5.13)$$

where s_0 is an arbitrary point and we obtain **dispersion relation with one subtraction**.

The real part of the elastic scattering amplitude can be measured experimentally via its interference between strong and electromagnetic (Coulomb) scattering at very small $|t|$. The discontinuities $\Delta A_1(s,t)$ and $\Delta A_2(s,t)$ at $t=0$ can be expressed via the total ab and $a\bar{b}$ cross sections. Say, in lab. frame we have

$$\Delta A_1(s) = 2p_a m_b \sigma_{ab}^{tot} \ , \tag{5.14}$$

$$\Delta A_2(s) = 2p_a m_b \sigma_{a\bar{b}}^{tot} \ , \tag{5.15}$$

and $s'-s = 2m_b(E'_a - E_a)$, $u'-u = 2m_b(E'_a + E_a)$ and for the real part of elastic ab amplitude we have

$$\begin{aligned} Re A_{ab}^{el} \ = \ & \sum_i \frac{a_i}{2m_b(E_i - E)} + \sum_j \frac{a_j}{2m_b(E_j - E)} + \\ & + \ \frac{2m_b}{\pi} \int_{m_a}^{\infty} \left[\frac{\sigma_{ab}^{tot}}{E' - E} + \frac{\sigma_{a\bar{b}}^{tot}}{E' + E} \right] \sqrt{E'^2 - m_a^2} dE' \ , \end{aligned} \tag{5.16}$$

where E_i and $E_j$are the lab energies that correspond to the bound states production, say

$$E_i = \frac{m_i^2 - m_a^2 - m_b^2}{2m_b} \ . \tag{5.17}$$

Dispersion relation can be compared with the experimental data. Its violation means the violation of as a minimum one of the underlying principles of elementary particle physics, namely

i) conservation of probabilities;

ii) micro-causality;

iii)Lorentz-invariance;

iv) structure of S-matrix singularities.

The real part depends on the integrals over total cross sections. It means that the precision measurement of the real part of elastic scattering amplitude give information about the behaviour of total cross sections at energies where direct measurements are impossible.

5.4 Dispersion relations for πp and pp scattering

Usually the ratio of the real to imaginary parts is considered

$$\rho_{hN} = \frac{ReA(s)}{ImA(s)} \ . \tag{5.18}$$

The comparison of the experimental data on the values of $\rho_{\pi^- p}$ with the calculations is presented in Fig. 12.

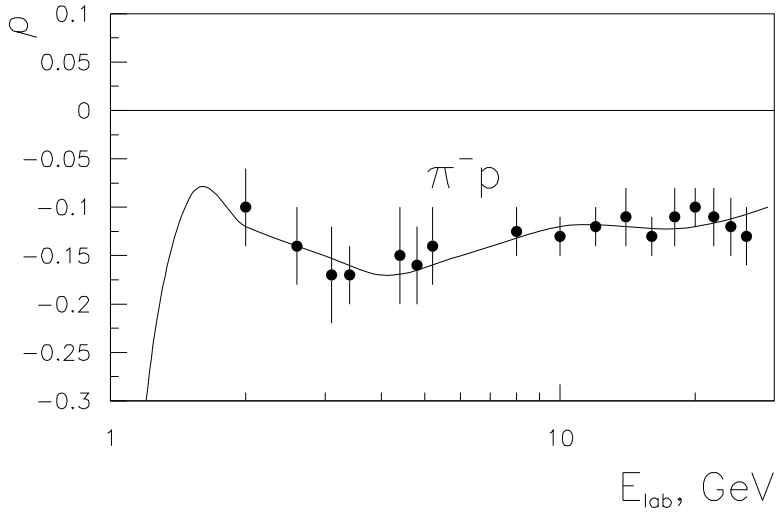

Figure 12: Comparison of $\frac{ReA(s)}{ImA(s)}$ experimental data for $\pi^- p$ elastic scattering (points) with the dispersion equation calculations shown by curve.

In the case of proton-proton elastic scattering the theoretical situation is more complicated. In s-channel there exist only cuts, the first one starts from the point $s = 4m_p^2$. However, in u-channel ($p\bar{p}$ scattering) we have one-pion pole at $u = m_\pi^2$, after that the cuts that correspond to the virtual production of 2π. 3π, etc. and only after, at larger u the elastic scattering cut that corresponds to $p\bar{p} \to p\bar{p}$ elastic scattering appears. So we have the pole and the unphysical discontinuity in the interval $4m_\pi^2 < u < 4m_p^2$ that is unknown experimentally.

Fortunately the contribution of this discontinuity to ρ_{pp} decrease at high energies as $1/s$ and it can be accounted for by the subtraction term at not very low energy. This unphysical discontinuity can create problems for the theoretical calculations only at comparatively low energies.

The comparison of the experimental data on the values of ρ_{pp} scattering with calculations is presented in Fig. 13.

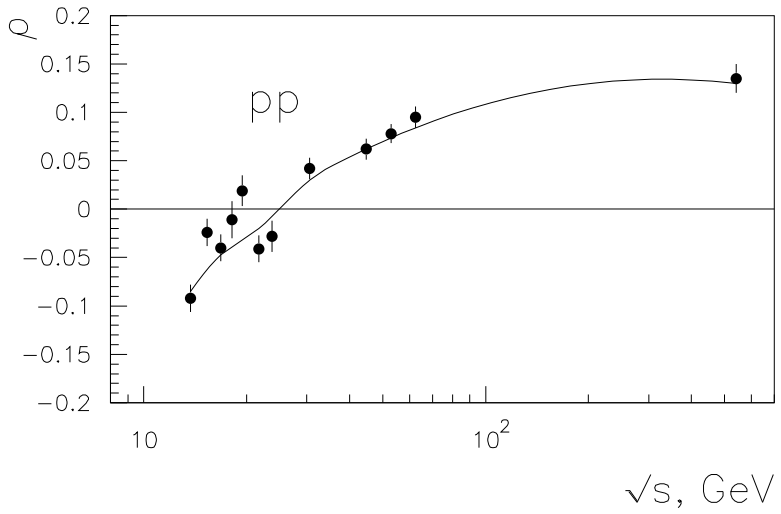

Figure 13: Comparison of $\frac{ReA(s)}{ImA(s)}$ experimental data for pp elastic scattering (points) with the dispersion equation calculations shown by curve.

6 Elastic and Inelastic Collisions at Different Energies

6.1 Hadron interactions in different energy regions

The hadron interaction processes can be divided (of course, rather subjectively) into the energy regions defined in Table 2:

low energy	$p_{lab} \leq$ (1.5 GeV/c
intermed. energy	$1.5 \leq p_{lab} \leq 30$ GeV/c
high energy	$8 \leq \sqrt{s} \leq 1000$ GeV
superhigh energy	$\sqrt{s} \geq 1$ TeV

Table 2. Hadronic interactions classified by energy regions.

At low energies the elastic scattering dominates, sometimes it can realize via s-channel resonances, i.e. via pole diagram.

At intermediate energies the structure of elastic hN interactions is rather complicated. Sometimes it is considered as a meson exchange in t-channel. The qusielactic processes become play an important role, when in the processes $1+2 \to 3+4$ one or both final particles are resonances. Also there exists a number of s-channel resonances, etc. and the processes of real multiparticle production start to appear. Due to all these the structure of elastic hN interactions is rather complicated.

At high energies the structure of interactions becomes simpler. The Regge-pole exchange phenomenology, which will be considered later provides a useful tool for the description of many quantitative features of high energy hadronic collisions and small momentum transferred.

At high momentum transferred different QCD approaches can be used.

For high energies $p_{lab} > 30$GeV, more than 80% of the total cross section is associated with processes in which new particles are produced. As the beam energy increases, the average number of the produced secondaries per inelastic event $< n >$ also increases firstly as $\sim \ln s$ and even more fast at higher energies. However, the number of secondaries produced on the unit of initial energy decrease with the growth of s.

All produced secondaries can be divided into two groups, fragmentation particles and centrally produced particles. The first ones carry out significant parts of the energy of the incident hadrons and their quantum numbers correlate with the quantum numbers of the incident hadrons, for example, in the case of a proton beam the fasters secondaries usually are proton and neutron. In the case of π^- beam the fragmentation production of secondary π^- or K^- is more probable than the production of π^+ or K^+. The reason is that rather often the fragmentation secondaries contain the valence quarks of incident particles. Centrally produced particles have rather small longitudinal momenta in c.m. frame, particles and antiparticles are

produced in equal portions and these particles contain only sea quarks produced in the collision.

The main part of produced secondaries are pions, the large fraction of them appears as a result of meson and baryon resonances decay. The number of produced K-mesons is significantly smaller than the number of pions, and the number of antibaryons is more smaller. For example, the ratios of particles produced in pp collisions at $\sqrt{s} = 200$ GeV in the central region are:

$$K^-/\pi^- \simeq 1/10 \ , \quad \bar{p}/\pi^- \simeq 1/20 \ . \qquad (6.1)$$

At superhigh energies the multiplicities of secondary particles increase and, at the same time the probability of hard processes such as gluon jet production becomes significant. The behaviour of cross sections in dependence on the initial energies is govered by **Froissart theorem**.

6.2 Neutral kaon regeneration

The processes in the system of neutral kaons present us very nice example of quantum effects in high energy physics.

From the point of view of strong interaction there exist two states, K^0 and $\bar{K}^0$ which have strangeness equal to +1 and -1, respectively. Strangness is conserved in strong interaction, so K^0 and $\bar{K}^0$ are different particles.

Free kaons decay via weak interaction, where strangeness is not conserved, but the CP-parity is approximately conserved (its violation occurs with very small probability).$K^0 = d\bar{s}$ and $\bar{K}^0 = \bar{d}s$ have no the definite values of CP-parity. From the point of view of decay we have two another system, K_s^0 with $CP = +1$, which decay into $\pi\pi$ with mean life time $0.9 \cdot 10^{-10}$ s and K_L^0 with $CP = -1$, which decay into 3π with mean life time $5 \cdot 10^{-8}$ s.

So from the point of view of hadrons (in strong interactions)

$$K^0 = \frac{(K_s + K_L)}{\sqrt{2}}\,, \quad \bar{K^0} = \frac{(K_s - K_L)}{\sqrt{2}}\,, \qquad (6.2)$$

and from the point of view of weak decay

$$K_s = \frac{(K^0 + \bar{K^0})}{\sqrt{2}}\,, \quad K_L = \frac{(K^0 - \bar{K^0})}{\sqrt{2}}\,. \qquad (6.3)$$

Now let us consider two interesting cases.

Below the threshold of $K^0\bar{K^0}$ pair production only K^0 can be produced, say in the low energy reactions $\pi^- p \to K^0\Lambda$ or $pp \to K^0\Lambda p$. However, K_s and K_L that consist K^0 in accordance with Eq. (6.2) will decay with their own mean life times presented above. At some distanse the number of K_L will be many times larger than the number of K_s, and, in accordance with Eq. (6.3) $\bar{K^0}$ will appear.

In the second case let us consider the kaon beam at significantly large distance from the production point, so all K_s decayed and we have pure K_L beam. Let this beam interacts with another extended target T, as it is shown in Fig. 14.

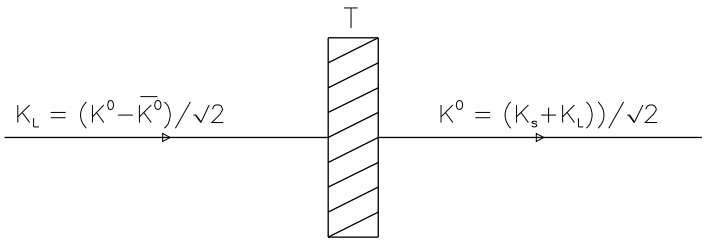

Figure 14: Regeneration of K-mesons.

In strong interactions we should consider separately the interactions of K^0 and $\bar{K}^0$. The absorption cross section of $\bar{K}^0$ in any target is larger in comparison with K^0 absorption cross section, so the main part of $\bar{K}^0$ will be absorbed and after the target we will have pure K^0 beam which consists of the equal part of K_s and K_L in agreement with Eq. (6.2). The process of appearance of K_s after a target is called **K-meson regeneration**.

6.3 Energy behaviour of hadron cross sections

In the energy region $\sqrt{s} = 5 - 50$ GeV the total cross sections of hN interactions are practically constant.

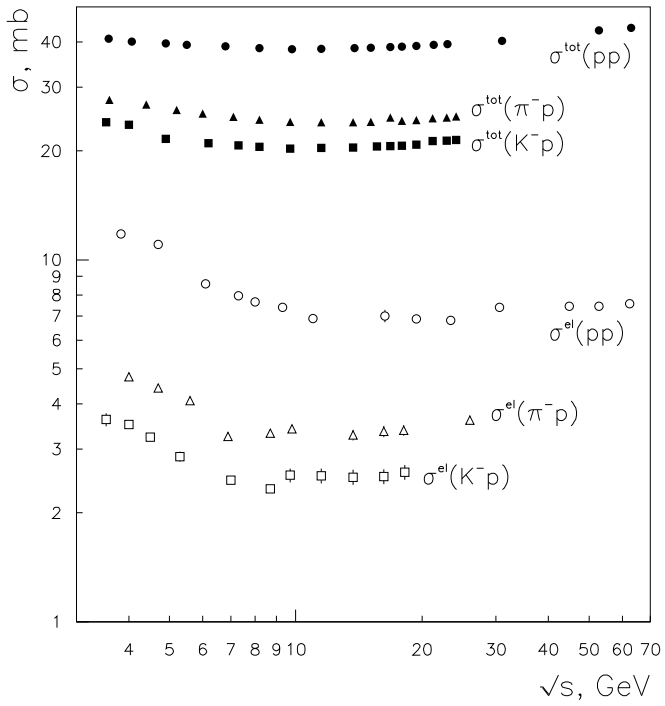

Figure 15: Total and elastic cross sections of pp, $\pi^- p$, and $K^- p$ collisions.

If one can see in more details, the total cross sections slightly decreaase at low energies and later srart to increase. The elastic cross sections repeate this behaviour.

At very high energies, see Fig. 16, there exist up to now only several experimental points for $\bar{p}p$ collisions obtained from colliders with rather large errorbars. However, they evidently show rather fast increase of this cross section with the energy.

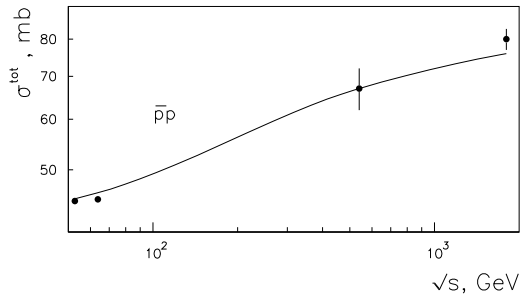

Figure 16: Total cross sections of $\bar{p}p$ collisions at very high energies.

Let us consider the energy independent behaviour of the total cross sections from the point of view that with the increase of the initial energy more and more new channels of secondary production are opened. The answer is that at the same time the cross sections of previously opened channels decrease. A schematic example is shown in Fig. 17: at $s = s_2$ the elastic scattering channel is open and the total cross section σ^{tot} is equal to the elastic cross section σ^{el}.

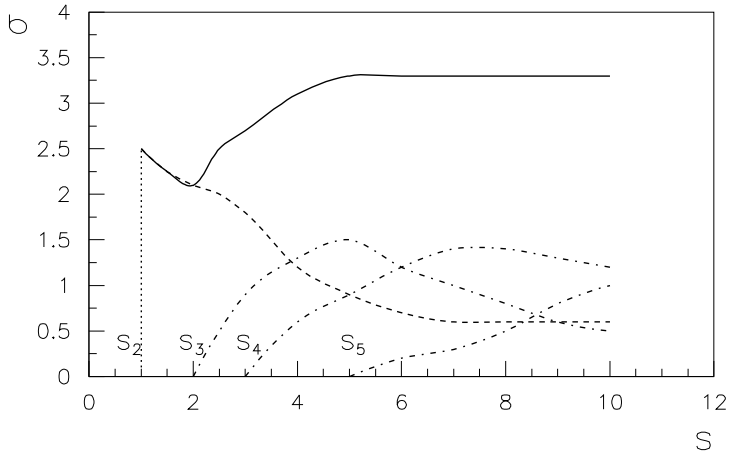

Figure 17: Energy dependence of total hadron-hadron cross section (solid curve) as a sum of elastic cross section (dashed curve) starting from threshold s_2 and several inelactic cross sections (dash-dotted curves) which start at thresholds s_3, s_4, and s_5.

In the case of pp collisions the first inelastic threhold ($pN\pi$ final state production) appears at $s = s_3 > s_2$. Next inelastic threholds (production of two, three,etc. pions) appear at $s = s_4$, $s = s_5$, etc., and increase of their cross sections are equilibrate by decrease of firstly of σ^{el}, after that by decrease of cross section of $pp \to pN\pi$ reactions, etc. It means that the cross section of every channel (of every **exclusive reaction**) can increases or decreases, but the sum of all these cross sections equal to the total cross section σ^{tot} is not changed.

At the same time some exclusive cross sections also can be energy independent in rather large energy region. The sinplest example are the elastic cross sections, in the region $\sqrt{s} = 5 - 30$ GeV we have

$$\frac{\sigma^{el}_{pN}}{\sigma^{tot}_{pN}} \simeq \frac{1}{6}\,, \quad \frac{\sigma^{el}_{\pi N}}{\sigma^{tot}_{\pi N}} \simeq \frac{1}{8}\,, \quad \frac{\sigma^{el}_{KN}}{\sigma^{tot}_{KN}} \simeq \frac{1}{10}\,. \tag{6.4}$$

Let us consider the differences of total cross sections of antiparticles and particles with protons. In all cases these differences are positive ones due to s-channel poles contributions in the cases of antiparticle interactions, namely there are a pion pole in $\bar{p}p$ scattering and nucleon pole in $\pi^- p$ scattering, whereas there are no s-channel poles in the cases of pp and only small number of poles in $\pi^+ p$ scattering.

The differences of $\sigma^{tot}_{\bar{p}p} - \sigma^{tot}_{pp}$, $\sigma^{tot}_{\pi^- p} - \sigma^{tot}_{\pi^+ p}$, and $\sigma^{tot}_{K^- p} - \sigma^{tot}_{K^+ p}$ measured experimentally at $p_{lab} > 35$ GeV/c that means $\sqrt{s} > 8$ GeV are presented in Fig. 18.

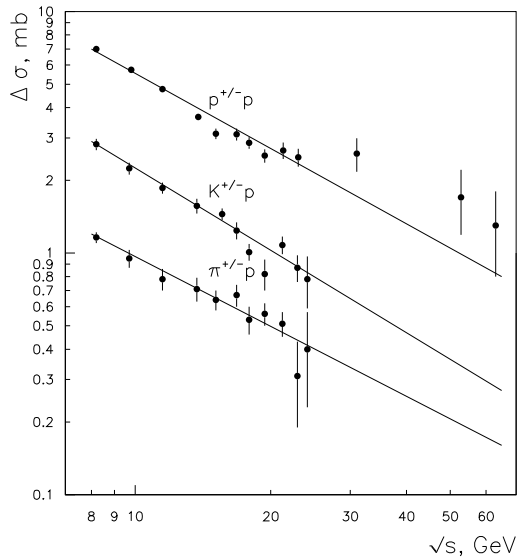

Figure 18: The differences of the total cross sections of $\bar{p}p - pp$, $\pi^- p - \pi^+ p$, and $K^- p - K^+ p$ collisions.

One can see that the differences of the presented cross sections decrease with the energy as the powers of s. It means that in the high energy region, the **Pomeranchuk theorem** which states that the total cross sections of particles and antiparticles are equal at asymptotically, high energies, is approximately fulfilled.

6.4 Limited transverse momenta of secondaries and Peyrou plot

The experimental fact is that in inelastic hadron-hadron interactions at high energy the produced particles have, as a rule, small transverse momenta (p_T) (of the order of their masses). At the same time the longitudinal momenta (p_L) can be as large as possible due to the energy conservation.

This situation can be shown in so-called **Peyrou plot**, where particle population is presented on the $p_L - p_T$ plane, see Fig. 19.

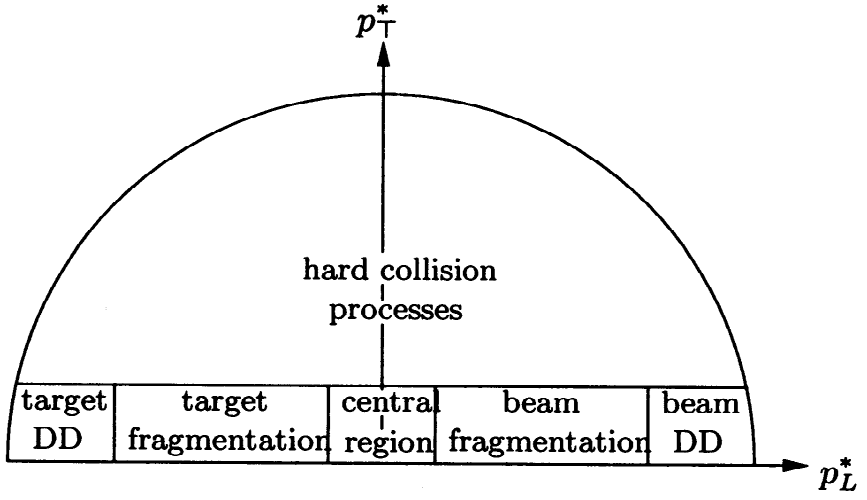

Figure 19: Peyrou plot defining various regions for a high energy collision (starred values refer to the c.m. frame).

The phase space boundary is shown by semicircle. The main part of secondary particle are placed below the horizontal line which schematically divide the regions of low and high p_T, i.e. in the regions of diffraction dissociation (DD in the Fig. 21), fragmentation regions, and central region, and only a few of them can be found in the region of hard (high p_T) collision processes.

However, the average values of transverse momenta are different for different secondaries, they increase with the mass of secondary particle. For example, in the central region of in pp collisions at $\sqrt{s} = 200$ GeV

$$\langle p_T \rangle_{\pi^-} \simeq 0.35\text{GeV/c} \ , \quad \langle p_T \rangle_{K^-} \simeq 0.53\text{GeV/c} \ , \quad \langle p_T \rangle_{\bar{p}} \simeq 0.6 \tag{6.5}$$

6.5 Multiperipheral collisions

The main properties of the soft multiparticle production at high energies are characteristic features of the **multiperipheral collisions picture**. At high energies the so-called ladder diagrams dominates, their rize and evolution are shown in Fig. 20.

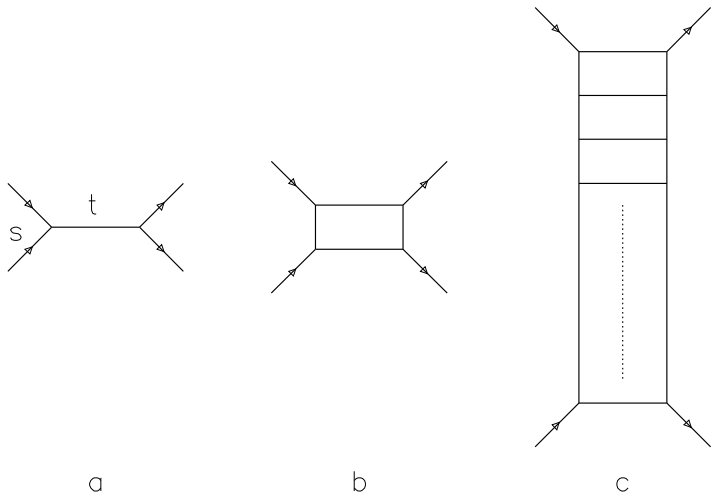

Figure 20: A sequence of t-channel ladder Feynman diagrams: (a) the single particle exchange Born approximation, (b) the box diagram, and (c) n-rung ladder.

The process of n-particle production in a high energy collision is shown in Fig. 21:

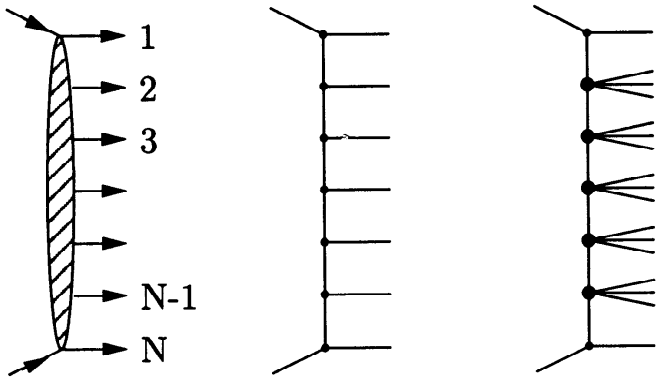

Figure 21: (a) Multiperipheral n-particle production process. (b) Cut-ladder multiperipheral diagram, and (c) cluster production multiperipheral diagram.

The ladder is called multiperipheral if all the secondaries can be ,enumerated in decreasing order of their longitudinal momenta:

$$p_{1L} \geq p_{2L} \geq ... \geq p_{nL} \ . \tag{6.6}$$

and all transverse momenta are small enough

$$p_{iT} \leq m_i \ . \tag{6.7}$$

In the multiperipheral processes all squares of the momentum transferred along the ladder t_i and squares of the adjacent invariant masses $s_{i,i+1}$ are limited as $s \to \infty$:

$$\begin{aligned} t_i &= (p_a - \sum_{k=1}^{i} p_k)^2 \\ &= (1 - \sum_{k=1}^{i} x_i)^2 \cdot (m_a^2 - \sum_{j=1}^{i} \frac{m_{jT}^2}{x_j})^2 - (\sum_{j=1}^{i} \mathbf{p}_{jT})^2, \end{aligned} \tag{6.8}$$

$$\begin{aligned} s_{i,i+1} &= (p_i + p_{i+1})^2 \\ &= (x_i + x_{i+1}) \cdot (\frac{m_{iT}^2}{x_i} + \frac{m_{(i+1)T}^2}{x_{i+1}}) \\ &- (\mathbf{p}_{iT} + \mathbf{p}_{(i+1)T})^2 \cdot \end{aligned} \tag{6.9}$$

6.6 Formation time

The important theoretical point is the existence of a formation time for secondary production.

IN QED the accelerated electron with energy E_e, velocity v_e and mass m_e emits the photons with wavelength λ from a distance

$$\lambda_f \simeq \frac{\lambda}{1 - v_e} \simeq \frac{\lambda}{2} \left(\frac{E_e}{m_e} \right)^2 \tag{6.10}$$

A similar example for strong interaction was demonstrated on a quantum mechanical level. Let us consider the case of deuteron–nucleus interaction, Fig. 22, with impact parameter b such that

$$R_A < b < R_A + R_d \; . \tag{6.11}$$

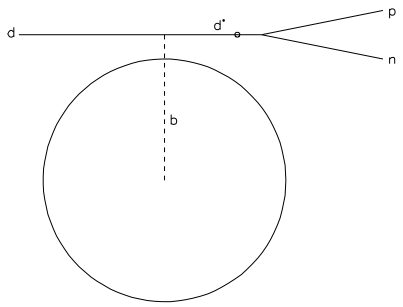

Figure 22: Fast deuteron disintegration in peripheral dA collision, b is the impact parameter.

If the transfer momenta are comparatively small. In this case both the deuteron ground state and its desintegration can occur. After the interaction we should expand the wave function of the final state d^* as superposition of deuteron and free proton and neutron:

$$\Psi_{d^*} = C_0\Psi_d + \sum_i C_i\Psi_{pn}^{(i)} \ , \ |C_0|^2 + \sum_i |C_i|^2 = 1 \ . \quad (6.12)$$

However, it is possible to write such superposition only at rather large time/distance, when nucleons in d^* state will interact. This needs a time of the order of R_d/v where v. So the state d^* can be determined as a deuteron or free $p+n$ state only at distance larger than

$$l_f = \frac{E_d}{m_d}\frac{R_d}{v} \quad (6.13)$$

This length is the formation length of the considered process. The value of R_d/v is of the order of 10 fm, so the formation length for relativistic deuterons with a large Lorenz-factor E_d/m_d can be many times larger than the nuclear radii. At the distances smaller than l_f we can not say anything about the nature of the state d^*.

All this can be extended and used for the explanation of multiple hadron production processes.

6.7 Secondary production in QCD

The simplest case of real QCD mechanism of secondary production is high energy e^+e^--annihilation.

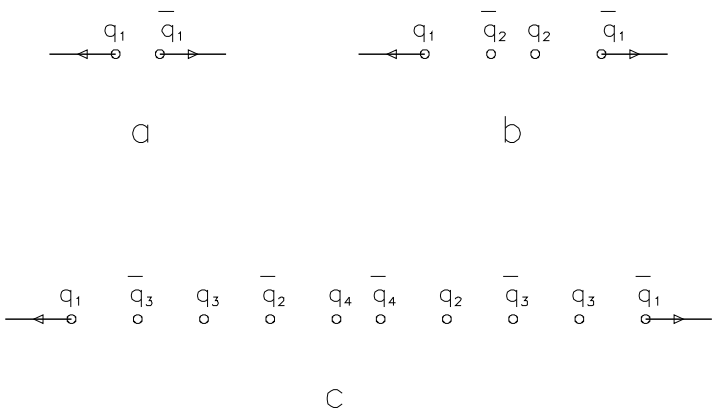

Figure 23: Multiple quark-antiquark pair production in e^+e^--annihilation that results in multiple production of secondary hadrons.

In the first step the virtual photon produces a quark-antiquark pair $q_1\bar{q}_1$ at small distance with large relative momentum, see Fig. 23a. When the distance between these two quarks becomes about 1 fermi (the confinement range), the tension of the colour field becomes so large that new quark-antiquark pair $q_2\bar{q}_2$ can be produced (Fig. 23b).

The probability that these four quarks will turn into two mesons (say, pions) is small. More probably several new quark-antiquark pairs $q_3\bar{q}_3$, $q_4\bar{q}_4$ and $q_5\bar{q}_5$ will be produced, that corresponds to the multiple production of secondaries, as it is shown in Fig. 23c, where five secondary mesons will be produced after hadronization of five quark-antiquark pairs. We will call such configuration of quarks a **coloured string**.

In the case of hadron–hadron inelastic interaction more probable is the production of gluon (octet) string $8\times\overline{8}$.

The most important characteristic for our consideration is that due to the confinement mechanism of secondary production we need about 1 fm longitudinal distance for the production of every quark-antiquark pair (*i.e.* for each secondary hadron). So, at high energies the space distance of secondary production can be about 10 fm, or even more, that is larger than the nucleus radius. It means that in the case of secondary production on nuclear target even without accounting the formation time effect, some part of secondaries will be produced outside the nucleus.

7 Regge-Gribov theory

7.1 Regge trajectories

Now we will consider the scattering theory in which the scattering amplitudes are analytically continued in the complex angular-momentum j-plane.

By analytically continuing the partial-wave amplitudes in angular momentum, one can represent the scattering amplitude as a sum of pole and cut contributions in the complex l plane. These singularities are related to the aymptotic behaviour of the scattering amplitude. The summation of ladder diagrams at high energies leads to the scattering amplitudes that contain so-called **Regge-trajectories**.

$$A(s,t) = \sum_i A_i \sim \sum_i g_i^2 \cdot s^{\alpha_i(t)} \ , \tag{7.1}$$

where Regge trajectory $\alpha_R(t)$ usually are written as

$$\alpha_R(t) = \alpha_R(0) + \alpha'_R \, t \ , \tag{7.2}$$

where $\alpha_R(0)$ (intercept) and α'_R (slope) are some numbers.

The integer values of $\mathrm{Re}\,\alpha_R(t)$ with $t > 0$ (non-physical region) correspond to the real particle exchange in t-channel with mass $M^2 = t$. So the notation of the trajectory usually coincides with that of the lowest mass hadron lying on this trajectory. The only exception is the Pomeron, the vacuum Regge trajectory with the highest intercept.

Regge trajectories have a special quantum number **signature**. The t-channel exchange by a Reggeon with positive signature ($\Theta = +1$) corresponds to the exchange by particles having even spin, for example, f and a_2, whereas the exchange by a Reggeon with negative signature ($\Theta = -1$) corresponds to the exchange by odd spin, for example ρ and ω particles.

The most important at high energies is the exchange by a Pomerons (vacuum Regge singularity).Unfortunately, until now we do not know the particles lying on the Pomeron trajectory.

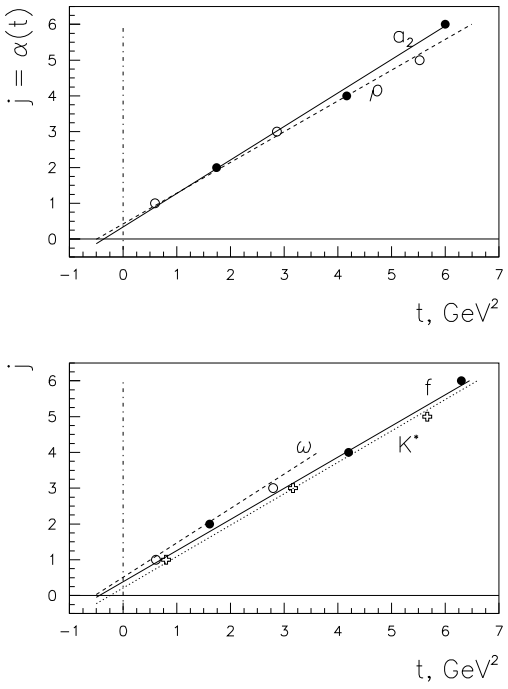

Figure 24: The Chew-Frautschi plot of $Re\alpha(t)$ versus t for the well established mesons with relatively large intercept. Upper panel: the particles lying on a_2 ($\Theta = +1$, solid line and closed points) and on ρ ($\Theta = -1$, dashed line and open points) trajectories. Lower panel: the particles lying on f ($\Theta = +1$, solid line and closed points) and on ω ($\Theta = -1$, dashed line and open points) and on K^* ($\Theta = -1$, dashed line and open crosses) trajectories.

The Reggeon parameters determined by the comparison with existing experimental data on high energy hadron collisions are presented in Table 3. It is necessary to note that these parameters depend on some model assumptions, so they are slightly different in different papers.

The experimental data show that all meson trajectories are approximately linear and they have approximately equal slopes $\alpha' \approx 0.8 \div 1$ GeV^{-2}; the slope α'_P is significantly less. The mass of the lightest particle that could lie on the Pomeron trajectory may be estimated with the help of α'_P; its quantum numbers should be $I^G = 0^+$, $J^P = 2^+$ and the mass about 2.7 GeV. Such a heavy hadron may probably be associated with a glueball state.

Baryon trajectories also exist, but their contributions have been studied in much less detail.

All well established hadrons lie on Reggeon trajectories at $t > 0$.

7.2 Regge pole exchange

One Regge pole exchange corresponds to the set of ladder diagrams where we sum over all possible numbers of rungs, see Fig. 25:

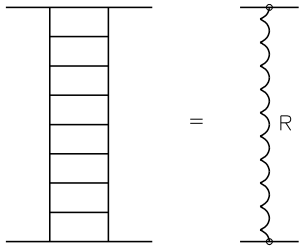

Figure 25: A ladder diagram which corresponds to exchange one Regge pole.

The contribution of a single t-channel Regge pole R to the amplitude of the process in Fig. 25 is given by :

$$A^R(s,t) = \gamma^R(t)\eta(\alpha_R(t))\left(\frac{s}{s_0}\right)^{\alpha_R(t)} \quad . \tag{7.3}$$

Here

$$\gamma^R(t) = \gamma_0^R e^{R_R^2 t} \tag{7.4}$$

is the coupling of Regge-pole which should be taken from experimental data.

$$\eta(\alpha_R(t)) = \frac{1 + \Theta_R e^{-i\pi\alpha_R(t)}}{\sin \pi\alpha_R(t)} \tag{7.5}$$

is the signature factor, where $\Theta_R = \pm 1$ is the signature, the quantum number connected with the sort of the Reggeon.

$$\eta(\Theta) = \begin{cases} i - \tan^{-1}(\frac{\pi\alpha_R}{2}) & \Theta = +1 \\ i + \tan(\frac{\pi\alpha_R}{2}) & \Theta = -1 \ . \end{cases} \tag{7.6}$$

Let us consider the most essential properties of the Reggeon exchange amplitude:

i. All energy dependence of $A^R(s,t)$ comes just from the factor $(s/s_0)^{\alpha_R(t)}$.

ii. $A^R(s,t)$ is an analytic function of s: its phase is uniquely determined. $A^R(s,t)$ is even (odd) under the crossing transformation $s \leftrightarrow u$, if the signature $\Theta_R = +1(-1)$.

iii. A significant property of the residue function $\gamma_R(t)$ is the factorization property:

$$\gamma_R(t) = g_R^{13}(t) g_R^{24}(t) \ . \tag{7.7}$$

The contribution of different Reggeon exchanges to the elastic scattering hp amplitudes are presented in Table 3.

Reaction	Regge singularities
$\mathrm{pp} \to \mathrm{pp}$	$A_P + A_f - A_\omega - A_\rho + A_{a_2}$
$\bar{p}\mathrm{p} \to \bar{p}\mathrm{p}$	$A_P + A_f + A_\omega + A_\rho + A_{a_2}$
$\pi^\pm\mathrm{p} \to \pi^\pm\mathrm{p}$	$A_P + A_f \pm A_\rho$
$\mathrm{K}^\pm\mathrm{p} \to \mathrm{K}^\pm\mathrm{p}$	$A_P + A_f \pm A_\omega \pm A_\rho + A_{a_2}$

Table 4. Regge poles which determine the elastic hp collisions at high energies

In linear combinations of the total cross sections, the contributions of some trajectories cancel, and the contributions of a single Reggeon can be isolated:

$$\Delta\sigma(\pi^\pm p) = \sigma_{tot}(\pi^+ p) - \sigma_{tot}(\pi^- p) = 2\gamma_\rho \left(\frac{s}{s_0}\right)^{\alpha_\rho(0)-1}. \tag{7.8}$$

Thus, the parameters of Reggeon intercepts $\alpha_R(0)$ and couplings γ_R for non-vacuum trajectories (ρ, ω, a_2, etc.) can be obtained via the fit of cross section differences.

The differential cross section of the elastic hN scattering can be parametrized in the form

$$\frac{d\sigma}{dt} = \frac{\sigma_{tot}^2}{16\pi}(1+\rho^2)e^{b(s)t} \,, \tag{7.9}$$

where ρ is the ratio of the real and imaginary parts of the amplitude, and the slope can be written as

$$b(s) = a_0 + 2\alpha'_{eff} \ln s/s_0 \,, \tag{7.10}$$

so the slope parameter logarithmically increases with the energy. A precise fit of small-t elastic cross sections with the inclusion of the Reggeon cuts and non-vacuum Reggeons gives the effective slope value $\alpha'_{eff} = 0.14 \pm 0.02$ GeV^{-2}.

7.3 Reggeon cuts, planar and non-planar diagrams

In Regge-Gribov theory there exist more complicate diagrams, first of all **Regge cuts** that are the absorptive corrections to Regge pole exchange. They arise from the exchange of two or more Reggeons:

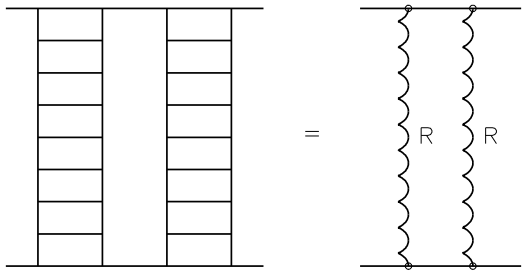

Figure 26: A two-ladder exchange diagram which corresponds to a Regge cut exchange.

However, the diagram in Fig. 26 considered as a Feynman-diagram gives zero contribution to the scattering amplitude. The reason comes from the space-time picture of strong interactions at high energy. The growth of characteristic longitudinal distances in strong interactions at high energies is quite evident. This effect reflects a very general feature of soft hadronic interactions.

Each hadron is considered to be surrounded by **vacuum fluctuations**, corresponding to the emission and absorption of virtual particles. Thus, a fast hadron with the momentum $k \gg m$ (m is a mass scale, say $m \sim m_\rho$), can be imagined as a cloud of particles – "partons" with different momenta. Then, the parton fluctuation can gather into a hadron, so that its Fock wave function approaches its asymptotic form, see Fig. 27a. Obviously, this requires a time of the order of k/m^2, k/m being the Lorentz factor and $1/m$ – the characteristic time of the interaction.

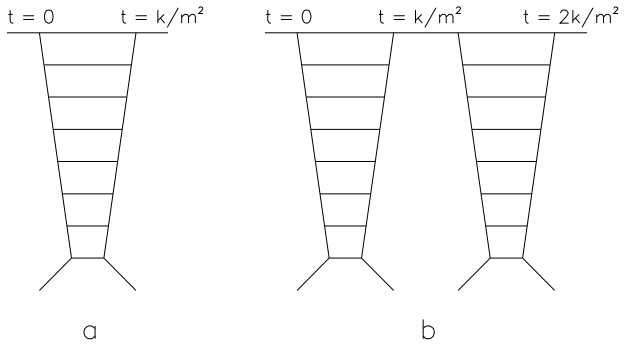

Figure 27: Interaction of a fast hadron with nucleon (a) and successive interaction with two nucleons (b) in the parton model.

The second interaction with a target needs again a time of the order of k/m^2 that seems to be impossible because a fast particle will be at large distance from a target.

In the language of Reggeon diagrams the simplest graph for the elastic scattering amplitude is the one-Pomeron exchange in Fig. 28a, which corresponds to a multiperipheral ladder of hadrons in the intermediate state, see Fig. 28b. The crosses mark the hadrons on the mass shell.

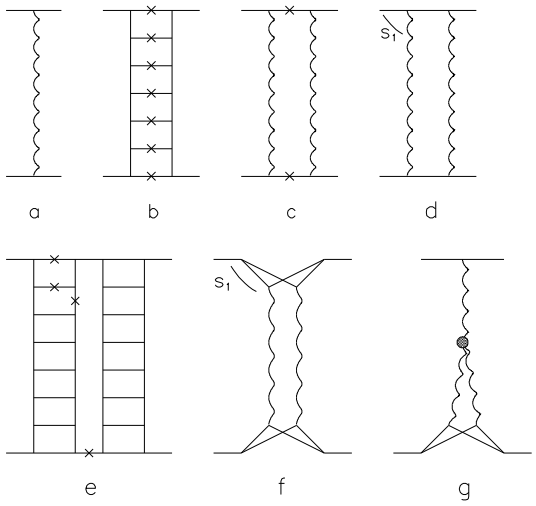

Figure 28: The Pomeron exchange (a) and its intermediate states (b). Planar (c-e) and non-planar (f,g) diagrams for the two-Pomeron cut.

The elastic cross section shown in Fig. 28c is one of the possible cuts of the diagram in Fig. 28d. The process in Fig. 28d is highly improbable at high energies since it corresponds to a repeated interaction with a point-like target. Thus, the amplitude in Fig. 28d should in fact vanish.

A large imaginary part in Fig. 28c is canceled by the cuts shown in Fig. 28e.

Non-zero corrections to the elastic amplitude come from the diagrams with the so-called Mandelstam crosses in Fig. 28f where both Pomerons interact simultaneously.

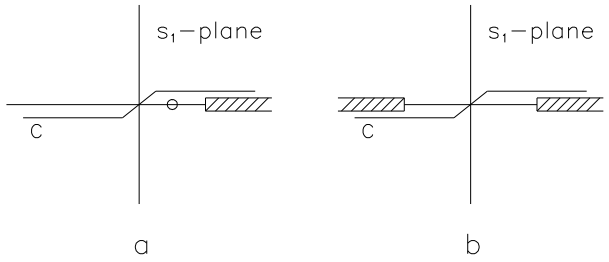

Figure 29: The integration contour C in the s_1-plane and singularities of the diagrams in Fig. 28d (a) and Fig. 28f (b).

The analytical properties of the diagrams in Fig. 28d and Fig. 28f are shown in Fig. 29. The amplitude in Fig. 28d has only a right discontinuity and a pole, both on the same side of the contour C as shown in Fig. 29a. A positive contribution of the pole is canceled by the negative contribution of the discontinuity.

Contrary to this, the amplitude in Fig. 28f has both left and right discontinuities, see Fig. 29b. Thus a nonzero answer follows.

7.4 Contribution of reggeon cuts in eikonal approximation

Let us consider the case when the exchanges by one and two Reggeons are possible, as it is shown in Fig. 30a, b, and c.

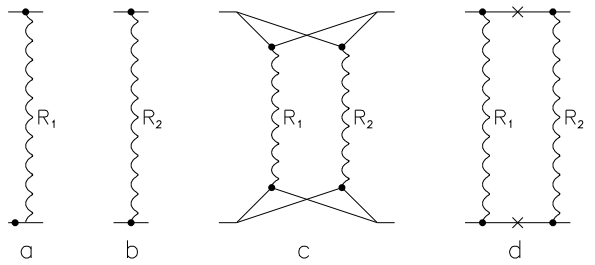

Figure 30: Elastic scattering amplitudes with exchange of one (a and b) and two (c) Reggeons. The eikonal approximation of the diagrams (c) is shown in (d).

The **eikonal approximation** means that we calculate the diagram Fig. 30d intead of Fig. 30c. The crosses in Fig. 30d mean that this particle is on mass-shell, i.e. we account for only a pole in Fig. 29a asuuming that the negative contribution of a cut in Fig. 29a and a positive contribution of a cut in Fig. 29b cancel each other.

After rather simple calculations we obtain

$$A^{el}(s,q^2) = A^{(1)}(s,q^2) + A^{(2)}(s,q^2)\ , \qquad (7.11)$$

$$A^{(1)}(s,q^2) = A_1(q^2) + A_2(q^2)\ , \qquad (7.12)$$

$$A^{(2)}(s,q^2) = \frac{i}{8\pi^2 s}\int d^2q_1 A_1(q_1)A_2(q-q_1)\ . \qquad (7.13)$$

The last integral is proportional to

$$\int d^2q_1 e^{-a_1 q_1^2} e^{-a_2(q-q_1)^2} = \frac{\pi}{a_1+a_2}\cdot exp\left[-\frac{a_1 a_2}{a_1+a_2}q^2\right]\ . \qquad (7.14)$$

Finally, the the amplitude $A^{el}(s,q^2)$ reads as

$$\begin{aligned} A^{el}(s,q^2) \ &= \ \gamma_0^{R_1}\eta_{R_1}\left(\frac{s}{s_0}\right)^{\alpha_{R_1}(0)} e^{-a_1 q^2} + \gamma_0^{R_2}\eta_{R_2}\left(\frac{s}{s_0}\right)^{\alpha_{R_1}(0)} e^{-a_2 \\ &+ \ \frac{i}{8\pi}\frac{\gamma_0^{R_1}\gamma_0^{R_2}}{a_1+a_2}\eta_{R_1}\eta_{R_2}\left(\frac{s}{s_0}\right)^{\alpha_{R_1}(0)+\alpha_{R_2}(0)-1}\cdot exp\left[-\frac{a}{a_1}\right. \end{aligned}$$

In the practically important case of Pomeron-Pomeron cut $\eta_P \simeq i$, the double exchange contribution has a negative sign.

Now we believe that the Pomeron trajectory

$$\alpha_P(t) = 1 + \Delta + \alpha'_P\, t\ ,\ \Delta > 0 \tag{7.16}$$

the one-Pomeron contribution to σ_{hN}^{tot} equals

$$\sigma_P = \gamma_0^P e^{\Delta\xi}\ , \xi = \ln s/s_0\ , \tag{7.17}$$

where γ_0^P is the Pomeron coupling, and σ_P rises with energy as s^Δ. To obey the s-channel unitarity, and the Froissart bound in particular, this contribution should be screened by the multipomeron discontinuities. An eikonal approximation yields

$$\sigma_{hN}^{tot} = \sigma_P f(z/2)\ , \tag{7.18}$$

where

$$\begin{aligned} f(z) &= \sum_{k=1}^{\infty} \frac{1}{k\cdot k!}(-z)^{k-1} = \frac{1}{z}\int_0^z \frac{dx}{x}(1-e^{-x}) \qquad (7.19)\\ z &= \frac{\gamma}{4\pi a_P} e^{\Delta\xi}\ ,\ a_P = R^2 + \alpha'_P\xi\ . \end{aligned}$$

Here R_P^2 is the radius of the Pomeron

At asymptotically high energies ($z \gg 1$) we obtain

$$\sigma_{hN}^{tot} = 8\pi\alpha'_P\Delta\xi^2\ , \tag{7.20}$$

according to the Froissart limit.

8 Diffractive Dissociation and Inclusive Reactions

8.1 Diffractive dissociation in hN collisions

At high energies a new class of processes appears – the diffractive dissociation of one or both colliding hadrons, see Fig. 31.

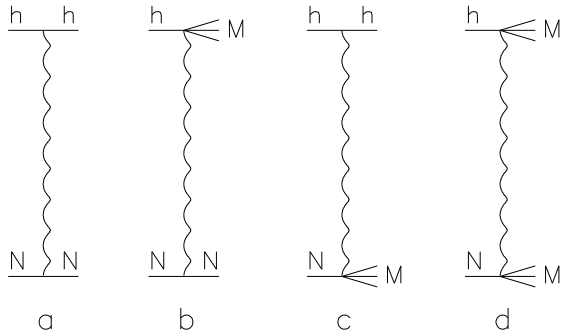

Figure 31: Regge-pole diagrams for elastic hN scattering (a), single diffractive dissociation of one colliding particle, (b) and (c), and double diffractive dissociation (d).

There exist single (Fig. 31b, 31c) diffractive processes, where one particle produces a diffractive jet and another is conserved, and a double diffractive dissociation (Fig. 31d), where both particles produce jets.

The integral cross sections of such processes are not large, but at high energies they generate new effects in inelastic collisions.

The contribution of the Pomeron exchange to the diffractive dissociation cross section is large, so these processes can exist even at asymptotically high energies.

The cross sections of single diffractive production σ_D at high energies can be estimated from the existing data. For the process of Fig. 31b the ratios of $R_D = \sigma_D/\sigma^{el}$ were found to be $R_D^{(p)} = 0.16 \pm 0.04$, $R_D^{(\pi)} = 0.37 \pm 0.12$ and $R_D^{(K)} = 0.42 \pm 0.2$.

The structure of the diffractive jet with mass M is the following. At small M it is saturated by resonance. The interference between resonance and background, or between two resonances with close masses can play here an important role.

An important feature of single diffraction dissociation processes is the existence of a minimal momentum transferred of the recoil particle, say a target nucleon in Fig. 31b. To calculate this, let us find the t value at zero transverse momentum ($p_{3T} = 0$) for the case $m_2 = m_4$ in the center-of-mass system,

$$t = (p_1 - p_3)^2 = (E_1 - E_3)^2 - (p_{1L} - p_{3L})^2 \ . \quad (8.1)$$

We use now

$$E_1 = \frac{s + m_1^2 - m_2^2}{2\sqrt{s}} \ , \ E_3 = \frac{s + m_3^2 - m_4^2}{2\sqrt{s}} \qquad (8.2)$$

and, for pure longitudinal momenta,

$$p_{iL} = \sqrt{E_i^2 - m_i^2} = E_i\sqrt{1 - m_i^2/E_i^2} \ . \qquad (8.3)$$

Let us expand these equations up to the second correction term, $\sqrt{1-x} = 1 - x/2 - x^2/8$. Assuming $p_{3T} = 0$ corresponding to the minimal value of t, we obtain

$$t_{min} = -m_2^2\frac{(m_3^2 - m_1^2)^2}{s^2} \ , \ M = m_3 \ . \qquad (8.4)$$

Clearly, for the case of elastic scattering $m_3 = m_1$, and $t_{min} = 0$.

The minimal longitudinal momentum p_{4L} of the recoil nucleon which appears due to the transfer of longitudinal momentum q_z, $q_z^2 = -t_{min}$. At high energies and $m_i^2 \ll M^2 \ll s$, in the laboratory system $s \simeq 2m_2E_{lab}$ and we obtain

$$q_z = p_{4L} = \frac{M^2 - m_1^2}{2E_{lab}} \ . \qquad (8.5)$$

8.2 Inclusive reactions

In inelastic high energy collisions many secondary particles can be produced. The reaction $a + b \rightarrow h_1 + h_2 + ... + h_n$, where all the secondaries are registered is called an **exclusive reaction**.

More often only one secondary particle h is registered and such processes

$$a + b \rightarrow h + X \tag{8.6}$$

are called **inclusive reactions**. X denotes all secondaries but h.

The inclusive cross section is defined as

$$F(s, p_L, p_T) = 2E\frac{d^3\sigma_h}{d^3p} \ . \tag{8.7}$$

The important variable isFeynman-x:

$$x_F = p^H/p^h_{max} \ , \tag{8.8}$$

where p^h_{max} is the kinematically maximum momentum of the incident hadron h; at high energies $p^h_{max} \simeq p_a$.

For the production of secondaries in the central region it turns out to be very convenient to use the variable

$$y = \frac{1}{2} \ln \frac{E + p_L}{E - p_L} = \ln \frac{E + p_L}{m_T} \simeq \ln 2xE_a/m_T \,, \tag{8.9}$$

called rapidity. The rapidity transforms additively under a Lorentz boost with a velocity $\beta = v/c$ along the beam axis:

$$y' = y - \frac{1}{2} \ln \frac{1+\beta}{1-\beta} \,. \tag{8.10}$$

In some high energy experiments only the angular distributions of the secondaries are measured and here the so-called pseudorapidity is used:

$$\eta = -\ln \tan(\theta/2) \simeq \ln 2xE_a/p_T \,, \tag{8.11}$$

and $\eta \simeq y$ for $y \geq 2 \div 3$.

There exists the exact equality

$$\frac{d\sigma(ab \to hX)}{dy} = x_E \frac{d\sigma(ab \to hX)}{dx_F} \,, \tag{8.12}$$

where $x_E = E_h/E_a$, E_a is the energy of the incident hadron a.

There are also several sum rules :

$$\int dx_F \frac{x_E}{\sigma_{ab}^{in}} \frac{d\sigma(ab \to hX)}{dx_F} = \langle K_h \rangle \ , \tag{8.13}$$

$$\sum_h \int dx_F x_E \frac{d\sigma(ab \to hX)}{dx_F} = \sigma_{ab}^{in} \tag{8.14}$$

(if the elastic $a + b \to a + b$ channel is not included) and

$$\int \frac{dy}{\sigma_{ab}^{in}} \frac{d\sigma_h}{dy} = \langle n_h \rangle \ , \tag{8.15}$$

where K_h is the part of the initial energy carried away by the secondary hadron h, $\Sigma \langle K_h \rangle = 1$, and $\langle n_h \rangle$ is the averaged multiplicity of h.

At high energies, multiperipheral production processes give the main contribution to the inelastic cross section that leads to the flat rapidity distribution in the central region.

8.3 Inclusive spectra at $x_F \to 0$ and $x_F \to 1$

At small x the x-dependence of $F(x, p_T)$ is negligible. The behavior of $F(x, p_T)$ in this region is determined by the multiperipheral diagram Fig. 32a.

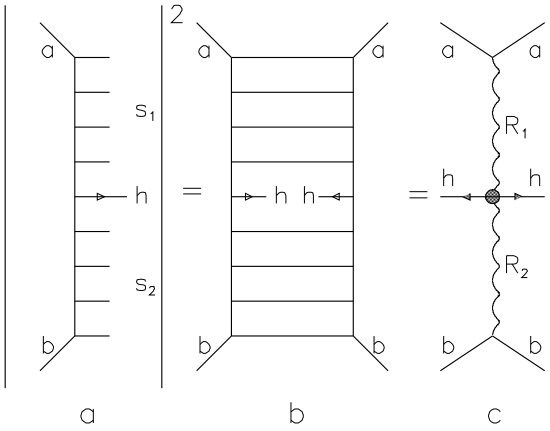

Figure 32: The modulo squared of the amplitude of inclusive production in the central region (a), (b) and the Regge-pole diagram for this reaction (c).

The inclusive production in the central region is determined as:

$$F(x, p_T) = \frac{1}{\pi^2 s} g^{aa}_{R_1}(0) g^{bb}_{R_2}(0) g^{hh}_{R_1 R_2}(p_T) \left(\frac{s_1}{s_0}\right)^{\alpha_{R_1}(0)} \left(\frac{s_2}{s_0}\right)^{\alpha_{R_2}(0)} , \tag{8.16}$$

$$s_1 = (p_a + p_h)^2 = m_T \sqrt{s} e^{-y^*} \tag{8.17}$$
$$s_2 = (p_b + p_h)^2 = m_T \sqrt{s} e^{y^*} .$$

The limit of x, close to unity, corresponds to the production of a diffractive beam with mass squared $M^2 \ll s$, see Fig. 33a. Now $x = 1 - M^2/s$. In the case of $M^2 \gg m^2$ the modulo squared of the graph Fig. 33a leads to the triple-Reggeon limit shown in Fig. 33b.

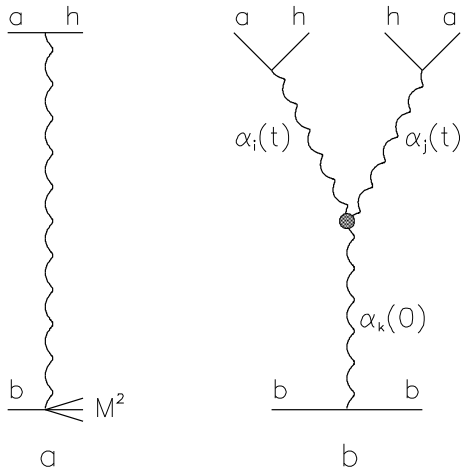

Figure 33: Secondary h production at $m_N^2 \ll M^2 \ll s$ (a) and modulo squared of this amplitude which corresponds to the triple-Reggeon diagram (b).

The triple-Pomeron term increases rapidly the inclusive spectrum at $x \to 1$.

8.4 The AGK cutting rules for Reggeon diagrams

The imaginary part of the elastic amplitude is written as a sum of several absorptive parts corresponding to all possible cuts of the given Reggeon diagram, each one related to a specific group of intermediate states via the s-channel unitarity. The one-Pomeron exchange gives a multiperipheral hadron ladder with small transverse momenta and the multiplicity $\sim \ln s$.

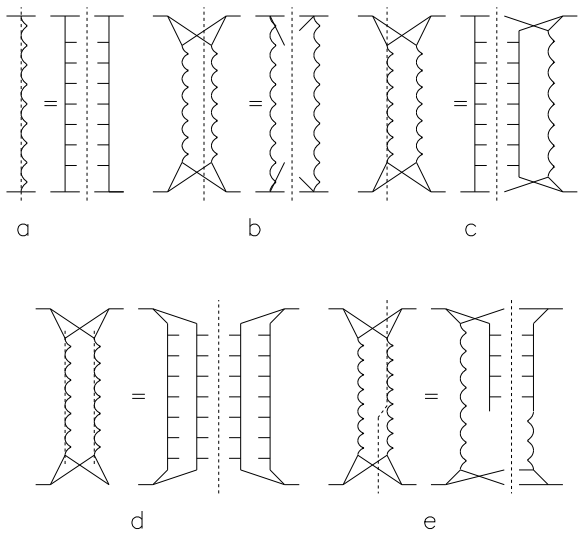

Figure 34: Various absorptive parts for the single (a) and double (b-e) Pomeron exchanges.

The contribution of the double Pomeron exchange to the elastic scattering amplitude is connected with three different types of intermediate states corresponding to the three possible cuts in Figs. 34b, 34c and 34d.

Consider a diagram with n Pomerons, yielding the contribution $(-1)^{n+1}S_n$ to the total cross section. The cross section for $\nu \leq n$ cut Pomerons is shown by simple algebra to be

$$\sigma^{(n,\nu)} = (-1)^{n+\nu}\frac{n!}{\nu!(n-\nu)!}2^{n-1}S_n \ , \ \nu \geq 1 \ , \quad (8.18)$$

$$\sigma^{(n,0)} = (-1)^n(2^{n-1}-1)S_n \ . \quad (8.19)$$

These relations are conventionally referred to as the **Abramovsky-Gribov-Kancheli (AGK) cutting rules**.

Obviously, the sum of all $\sigma^{n,\nu}$ equals S_n for each $n \geq 1$

$$\sum_{\nu=1}^{n} \sigma^{(n,\nu)} + \sigma^{(n,0)} = S_n(-1)^{n+1} \ . \quad (8.20)$$

The sum $\Sigma_{n=\nu}^{\infty}\,\sigma^{(n,\nu)}$ for a fixed ν gives the total cross section for a specific physical process – the production of ν ladders of secondary particles.

$$\sigma^{(\nu)} = \sum_{n=\nu}^{\infty} \sigma^{n,\nu} = \frac{(-1)^{\nu}}{\nu!} \sum_{n=\nu}^{\infty} \frac{n!}{(n-\nu)!}(-1)^{n} 2^{n-1} S_n \ . \tag{8.21}$$

The AGK cutting rules yield several important relations for inclusive production. For example, consider the multiplicity of a secondary hadron h with given quantum numbers in the central region of the spectrum, $n_h(x_F \to 0)$.

Multiplying the probability for each process by the corresponding multiplicity, one obtains

$$n_h(x=0) = n_h^{(1)} \sum_{\nu=1}^{\infty} \nu\sigma^{(\nu)} / \sum_{\nu=1}^{\infty} \sigma^{(\nu)} = n_h^{(1)} S_1 / \sum_{\nu=1}^{\infty} \sigma^{(\nu)} \tag{8.22}$$

i.e. the diagram with a one-Pomeron exchange S_1 is the only one contributing to the multiplicity (to the inclusive spectrum) in the central region. Contributions of various absorptive parts in an arbitrary diagram with $n \geq 2$ cancel each other.

9 Hard Processe in Hadron Interactions and Parton Distributions

9.1 Connection between hadron-hadron and quark-gluon interactions

QCD describes the hard processes that occur in hadron-hadron collisions, on the level of hard interactions of **partons** – quarks and gluons. As the examples of such processes we can present production of high-p_T hadron jets, heavy particles ((charmed and beauty hadrons, W and Z bosons), high mass Drell-Yan ($\mu^+\mu^-$) pairs, high-p_T (direct) photons, etc.

QCD is a theory for quark-gluon interactions, whereas the experimental data are obtained in hadron-hadron collisions. Usually the standard **factorization expression** is used for the cross section of a hard process in a hadron a-hadron b collision has the form

$$\begin{aligned}\sigma^{ab}_{hard} &= \int_{x_{10}}^1 \frac{dx_1}{x_1}\int_{x_{20}}^1 \frac{dx_2}{x_2}\left[x_1 G_{a/1}(x_1,\mu^2)\right]\times \\ &\times \left[x_2 G_{b/2}(x_2,\mu^2)\right]\hat{\sigma}^{hard}(\hat{s},\mu^2)\ ,\end{aligned} \tag{9.1}$$

where $x_{10} = \hat{s}_{min}/s$ and $x_{20} = \hat{s}_{min}/(sx_1)$.

Eq. (9.1) should account for all possible hard subprocesses in the considered order of α_s. For example, the LO heavy quark pair production cross section in hadron-hadron collision should account for the contributions of four diagrams presented in Fig. 35.

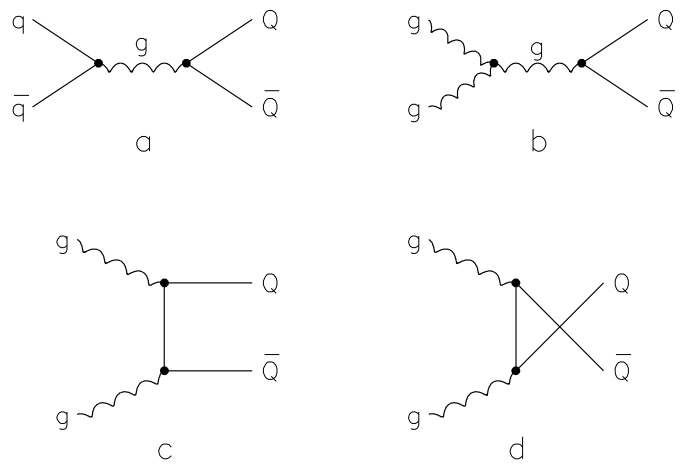

Figure 35: Low Order parton model diagrams for heavy quark production via quark-antiquark (a) and gluon-gluon (b, c, d) fusion.

The parton cross section $\hat{\sigma}^{hard}(\hat{s}, \mu^2)$ should be calculated in accordance with Feynman rules for QCD diagrams.

In the simplest approach of QCD – **parton model** – all quarks and gluons involved are assumed to be on mass shell, having only longitudinal component of the momentum **collinear approximation** and the cross section is averaged over two transverse polarizations of the gluons. The virtualities q^2 of the initial partons are taken into account only through their densities.

The cross sections of hard processes depend significantly on the quark and gluon structure functions. These functions are practically unknown experimentally for very small values of x.

9.2 Deep inelastic scattering and its variables

The most important information about internal structure of a nucleon can be obtained from deep inelastic *ep* scattering. Just in these experiments it was proved in sixties that inside a proton there exist point-like electrically charged particles – partons.

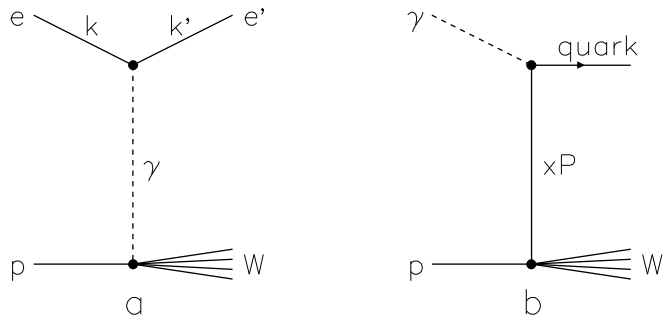

Figure 36: Deep inelastic *ep* scattewring (a) and the process of virtual photon absorption by a quark with $x = Q^2/(W^2 + Q^2)$.

The cross section of the process $ep \to eX$, Fig. 36a, depends on two structure functions, $F_1(x, Q^2)$ and $F_2(x, Q^2)$:

$$\frac{d^2\sigma}{dxdy} = \frac{4\pi\alpha^2(s-m^2)}{Q^4}[(1-y)F_2(x,Q^2) + \quad (9.2)$$
$$+ \; y^2 F_1(x,Q^2) - \frac{m^2}{s-m^2}xyF_2(x,Q^2)] \; ,$$

where m is a proton mass.

$$\nu = (qp)/m \quad (9.3)$$

is the virtual photon energy in the lab. frame, $s = (k+p)^2$ - total energy of the process,

$$W^2 = (q+p)^2 = m^2 + 2m\nu - Q^2 \quad (9.4)$$

is the mass squared of the system recoiling against the lepton,

$$x = \frac{Q^2}{2(pq)} = Q^2/(W^2+Q^2) \simeq Q^2/(W^2+Q^2) \quad (9.5)$$

is Bjorken variable,

$$y = (qp)/(kp) = \nu/E \quad (9.6)$$

- the fraction of the lepton energy lost in the lab. frame.

If electrically charged partons have spin 1/2 (they are quarks),

$$F_2(x, Q^2) = 2xF_1(x, Q^2) \ . \tag{9.7}$$

Let us calculate which quark can absorb the photon with given Q^2 and ν. The masses of light quarks are negligibly small, so $(q + xp)^2 = 2x(qp) - Q^2 = 0$ and $x = Q^2/(2m\nu)$. It means that only a quark having the x fraction of the proton momentum in a frame where the proton momentum is large can absorb the virtual photon in the process with given Q^2 and ν. So the cross section of a virtual photon absorption gives the information about quark distributions.

In Leading α_s Order (LO) QCD a proton structure function $F_2(x, Q^2)$ can be expressed in terms of **parton distributions** $f_i(x, Q^2)$:

$$F_2(x, Q^2) = \sum_i e_i^2 f_i(x, Q^2) \ . \tag{9.8}$$

The parton distributions $f_i(x, Q^2)$ are the probabilities that a parton of type i (quark, antiquark or gluon) carries a proton momentum fraction x in a frame where the proton momentum is large.

9.3 Evolution equation for parton distributions

The (GLDAP) evolution equation is used usually for extraction the quark and gluon distributions from the experimental data. It sums up in leading logarithm approximation (LLA) all the QCD diagram contributions proportional to $(\alpha_s \ln q^2)^n$.

The conventional GLDAP evolution equations for quark $q(x,Q^2)$ and gluon $G(x,Q^2)$ distributions can be written in the form

$$\frac{dq^i(x,Q^2)}{d\ln Q^2} = \frac{\alpha_s(Q^2)}{2\pi}\int_x^1 \frac{dy}{y}[q^i(y,Q^2)P_{qq}(\frac{x}{y}) + + G(y,Q^2)P_{qG}(\frac{x}{y})] , \tag{9.9}$$

$$\frac{dG(x,Q^2)}{d\ln Q^2} = \frac{\alpha_s(Q^2)}{2\pi}\int_x^1 \frac{dy}{y}[\sum_{i=1}^{2n_f} q^i(y,Q^2)P_{Gq}(\frac{x}{y}) + + G(y,Q^2)P_{GG}(\frac{x}{y})] . \tag{9.10}$$

In LO the **running QCD constant**

$$\alpha_s(Q^2) = \frac{12\pi}{(33 - 2n_f) \ln Q^2/\Lambda^2_{QCD}} \,, \qquad (9.11)$$

where the value of the parameter Λ_{QCD} depends on the value of n_f, i.e. on the assumption how many quarks can be considered as massless ones. Usually $n_f = 3$ is used If the values of Q^2 are not very large and in this case $\Lambda_{QCD} \sim 250$ MeV. In the case of more precise calculations (Next-to Leading Order, etc.) the value of Λ_{QCD} changes, but not too strong.

The kernels $P_{qq}(z)$, $P_{qG}(z)$, $P_{Gq}(z)$ and $P_{GG}(z)$ correspond to the possibility of the transitions:

(i) quark into quark with emission a gluon,

(ii) gluon into quark-antiquark pair,

(iii) gluon production by a quark and

(iv) gluon production by gluon via the triple gluon vertex.

At small Q^2 besides the GLDAP contribution to structure functions there exist many another contributions, such as non-perturbative ones, etc. Many sets of parton distributions are obtained by the following way: the boundary conditions are written at some $Q^2 = Q_0^2$, which can be considered as large enough (usually Q_0^2 is 4-5 GeV^2) in agreement with the existing experimental data, and then the structure functions at $Q^2 > Q_0^2$ are obtained using GLDAP equation:

$$\begin{aligned} xq^i(x,Q^2) &= xq^i(x,Q_0^2) + \int_{\ln Q_0^2}^{\ln Q^2} d\ln Q_1^2 \times \\ &\times \frac{\alpha_s(Q_1^2)}{2\pi} \int_x^1 \frac{dy}{y} [q^i(y,Q_1^2) P_{qq}(\frac{x}{y}) + \\ &+ G(y,Q_1^2) P_{qG}(\frac{x}{y})] \ , \end{aligned} \tag{9.12}$$

$$\begin{aligned} xG(x,Q^2) &= xG(x,Q_0^2) + \int_{\ln Q_0^2}^{\ln Q^2} d\ln Q_1^2 \times \\ &\times \frac{\alpha_s(Q_1^2)}{2\pi} \int_x^1 \frac{dy}{y} [\sum_{i=1}^{2n_f} q^i(y,Q_1^2) P_{Gq}(\frac{x}{y}) + \\ &+ G(y,Q_1^2) P_{GG}(\frac{x}{y})] \ , \end{aligned} \tag{9.13}$$

9.4 Boundary conditions and gluon distributions at small x

The integral representation of GLDAP Eqs. allow one to calculate the Q^2-dependences of the parton distributions if they are known at some value $Q^2 = Q_0^2$ as the functions of x.

The so-called "dynamical" generation of parton distributions seems to be very attractive. The first attempts tryed to generate all gluon and sea quark distributions purely dinamically, as a results of parton evolution starting from only valence quark distributions at $Q^2 = Q_0^2$, i.e. with the extreme boundary condition at $Q_0^2 \sim \Lambda_{QCD}^2$:

$$xG(x, Q_0^2) = x\overline{q}(x, Q_0^2) = 0 \qquad (9.14)$$

without any free parameters. This approach works qualitatively well and yields, in particular, the remarkable prediction for the momentum fraction $\langle x \rangle_g$ carried by gluons,

$$\langle x \rangle_g = \int_0^1 xG(x, Q^2)dx = 0.45 \qquad (9.15)$$

at $Q^2 = 1$ - 5 GeV^2 without using any parameters.

However, quantitatively the obtained gluon and sea quark distributions are in contradiction with the experimental data. These distributions are too soft at comparatively large x and too steep in the small x region.

So, one can use the boundary conditions

$$xG(x,Q_0^2) = Ax^{\alpha}(1-x)^{\beta}\ , \tag{9.16}$$

$$x\overline{q}(x,Q_0^2) = Bx^{\gamma}(1-x)^{\delta} \tag{9.17}$$

with $\alpha > 0$ and $\gamma > 0$ at small enough $Q^2 = Q_0^2$ and we can be sure that all parton distrinbutions at $Q^2 > Q_0^2$ will be positive at all x.

The presented scheme is known as the Double Leading-Logarithm Approximation (DLLA) as it sums the leading power of $\ln Q^2$ and $\ln(1/x)$. That is, for each additional factor of α_s, we keep only the $\ln(Q^2)\cdot\ln(1/x)$ term accompanying that α_s.

It is useful to give a simple diagrammatical explanation of the DLLA. The leading double logarithms at large Q^2 and small x are generated by the diagrams of Fig. 37a in which the gluons have strongly ordered transverse momenta

$$Q^2 \gg k_T^2 \gg k_{nT}^2 \gg ... \gg k_{2T}^2 \gg k_{1T}^2 \gg Q_0^2 \ . \tag{9.18}$$

The longitudinal momenta in the DLLA are also ordered :

$$x < x_n < ... < x_2 < x_1 \ . \tag{9.19}$$

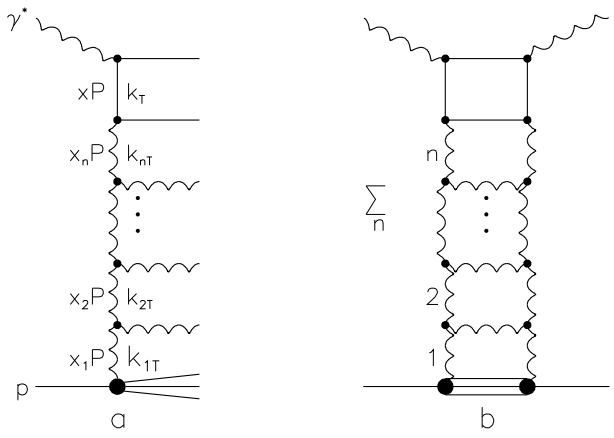

Figure 37: Diagrammatic representation for probing the gluon content of the proton at high Q^2. On squaring the amplitude (a)we obtain a ladder diagram (b).

Thus as we proceed along the chain from the proton momentum p towards that of the probe γ^*, the proton is split into smaller and smaller pieces.

In each loop the integration over the transverse momentum is logarithmical (dk_{iT}^2/k_{iT}^2) and the strong ordering generates a $(\ln Q^2)^n/n!$ behaviour.

Thus we say that the DLLA is generated by the sum of gluon ladder diagrams of the type of with strongly ordered transverse and longitudinal momenta.

In the region of very small x an additional problem appears. The DLLA equation neglects, by definition, those terms in the perturbative expansion which contain the leading power of $\ln(1/x)$ but which not accompanied by the leading power of $\ln Q^2$.

The accounting for these terms gives the gluon distribution at $x \to 0$ in the Balitskij-Fadin-Kuraev-Lipatov (BFKL) form

$$xG(x, Q^2) \sim h(Q^2) \cdot x^{-\lambda_{max}} \ , \qquad (9.20)$$

where

$$\lambda_{max} = \frac{3\alpha_s}{\pi} 4 \ln 2 \ . \qquad (9.21)$$

One can see that $xG(x, Q^2)$ grows rapidly with increasing $\ln(1/x)$ at fixed Q^2.

10 Nuclear Shapes

10.1 Nuclear structure, protons, neutrons, meson currents

The atomic nucleus is usually a sphere which contains nucleons: protons and neutrons.Light nuclei contain approximately equal numbers of protons and neutrons, whereas the number of neutrons in heavy nuclei is about 1.5 times larger than the number of protons, mainly due to the Coulomb repulsion contribution to the total binding energy.

The binding energy of nucleons in nuclei (except in the lightest ones) is about 8 MeV per nucleon, i.e. by two orders of magnitude smaller than the nucleon masses. So the Fermi motion of the nucleon is a non-relativistic one, and the high-momentum tail of the nucleon motion is relevant just in a few cases.

Nuclear matter is not distributed uniformly even in spherical nuclei; its radial distribution is rather complicated, being a real function of the radial variable r – the distance from the center.

It is, however, quite reasonable to introduce the "effective" nuclear radius R_A, and the experimental data show that for not very light nuclei these radii can be described by the rather simple dependence

$$R_A = R_0 A^{1/3} \, , R_0 = 1.1 \div 1.3\text{fm} \, . \qquad (10.1)$$

The radii of most of the individual nuclei vary, as a rule, within the presented limits.

We can see here the serious problem for our future considerations. Protons and neutrons should be bound by meson exchanges. The number of required mesons is rather large, of the order of ten. As the pion is the lightest meson, it must give a significant contribution, especially at large distances ($\sim 1/m_\pi$); this is in beautiful agreement with Yukawa's estimation of the range of strong interactions. So we can expect that nuclei consist of nucleons and mesons. If so, our fast particle (probe) can sometimes interact with a target meson, different from the meson belonging to the individual nucleon.

However, nobody ever saw such a reaction.

10.2 Elastic eA-scattering and nuclear form factors

High energy elastic eA scattering can be used for investigation of nuclear structure.

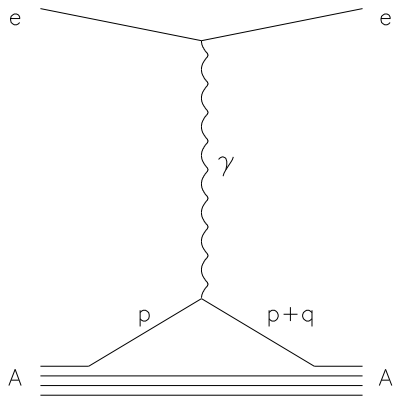

Figure 38: Elastic eA scattering in Born approximation.

If q is the momentum transferred from the electron to the nucleus via one-photon exchange, R_Z is the average electric radius of the nucleus, and $qR_Z \gg 1$ (i.e. the photon can interact with only one nuclear proton), we obtain the matrix element of such scattering as

$$M \propto \int \psi_Z(p)\psi_Z^*(p+q)d^3p \,, \qquad (10.2)$$

where $\psi_Z(p)$ and $\psi_Z^*(p+q)$ are the scattered proton wave functions before and after the scattering.

Taking into account that

$$\psi_Z(p) = \int \psi_Z(r) e^{ipr} d^3r \ , \ \psi_Z^*(p+q) = \int \psi_Z^*(r) e^{-i(p+q)r} d^3r \ , \tag{10.3}$$

we obtain

$$M \sim \int |\psi_Z(r)|^2 e^{-iqr} d^3q \ . \tag{10.4}$$

The expression for a one-particle charged nuclear form factor reads

$$G_Z(q) = \int \rho_Z(r) e^{-iqr} d^3r \ , \ G_Z(0) = 1 \ , \tag{10.5}$$

where the distribution of charged nuclear density is $\rho_Z(r) = |\psi_Z(r)|^2$.

It is clear now that the cross section of the elastic eA scattering is proportional to $G_Z^2(q)$; from measurements of such cross sections at different q we can obtain information about the charged nuclear density distribution $\rho_Z(r)$.

In the case of $qR_Z \leq 1$ the probing electron can interact with several nucleons or even with a whole nucleus. This can result in either one-particle or collective nuclear excitations related to the subject of classical nuclear physics.

10.3 Hofstädter experiments and the geometry of the nucleus

The first detailed information about nuclear charge density distributions comes from the experiments of R. Hofstädter on high energy eA scattering. Different models for charge density distributions were used for the analyses, including the point-like model $\rho(r) = \delta(r)$, uniform, Gaussian, exponential and some other distributions; some of them give rather similar numerical results. First of all, it was observed that the point-like model can be excluded, the nuclei being best characterized by form factors.

A reasonable fit of the nuclear form factors can be obtained using the Fermi (Woods-Saxon) distribution

$$\rho_A(r) = \frac{\rho_1}{1 + e^{(r-c)/a}} \, , c \gg a \, . \qquad (10.6)$$

Here ρ_1 is the normalization constant, c is a parameter measuring the nuclear size and a is related to the diffuseness of the surface, in other words, to the thickness of the nuclear "skin".

This distribution is shown in Fig. 39 in more detail. The parameter c shows the value of r at which $\rho(r)$ decreases twice compared to $\rho(r = 0)$, $\rho(r = c) = 0.5\,\rho(r = 0)$. The value of a determines the distance $a_1 = 4\,a\ln 3 \sim 4.4\,a$, where $\rho(r)$ decreases from $0.9\,\rho(r = 0)$ to $0.1\,\rho(r = 0)$.

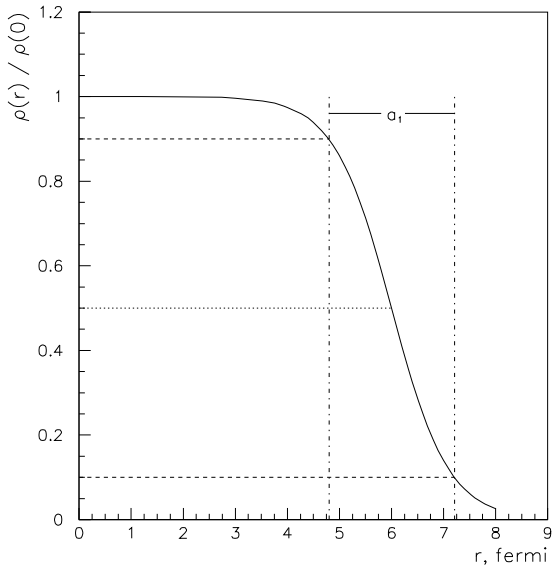

Figure 39: Woods-Saxon distribution, Eq. (10.7), with $c = 6$ fm and $a_1 = 4a\ln 3$, with $a = 0.55$ fm.

We will also use

$$\langle R_A^2 \rangle = 4\pi \int_0^\infty \rho(r) r^4 dr \ , \qquad (10.7)$$

or its square root.

The parameters of several nuclei are presented in Table 7.

Nucleus	r.m.s. radius	R_{eq}	$r_0 = \frac{R_{eq}}{A^{1/3}}$	$r'_0 = \frac{c}{A^{1/3}}$
Ca^{40}	3.52	4.54	1.32	1.06
V^{51}	3.59	4.63	1.25	1.07
Co^{59}	3.83	4.94	1.27	1.05
In^{125}	4.50	5.80	1.19	1.08
Au^{197}	5.32	6.87	1.18	1.10
Bi^{209}	5.52	7.13	1.20	1.09

Table 7. Some parameters in fm) of the nuclear density distribution. R_{eq} is the radius of the equivalent uniform model.

In the case of light nuclei (^{9}Be, ^{12}C, ^{16}O) a Gaussian parametrization can also be used:

$$\rho_A(r) = (\alpha^2/\pi)^{3/2} e^{-\alpha^2 r^2} \ , \tag{10.8}$$

$$1/\alpha^2 = \frac{2}{3}\langle R_A^2 \rangle. \tag{10.9}$$

Such a parametrization allows to calculate analytically many expressions related to the scattering on nuclear target.

11 Cross Sections of Hadron-Nucleus Scattering

11.1 Eikonal approximation and Glauber theory

The case of hadron–nucleus interactions is more complicated compared to eA scattering due to the possibility of multiple interactions. A good formalism for this is the Glauber theory which comes from quantum mechanics.

The basis is the **eikonal approximation** for fast particle scattering in quantum mechanics. Let a fast particle with momentum k and kinetic energy T in laboratory frame scatter on the nucleus A, which we treat for the moment as a collection of potential wells of the size a and of the depth V_0.

Provided the following conditions

$$ka \gg 1 \ , \ T/V_0 \gg 1 \tag{11.1}$$

are satisfied, the characteristic scattering angles are small and thus the phase shift $\chi_A(b)$ is given by the integral of the total nuclear potential :

$$\chi_A(b) = -\frac{m}{k} \int_{-\infty}^{\infty} dz \, V_A(b,z) \ , \tag{11.2}$$

b being the impact parameter (2-dimensional vector). Due to the conditions (11.1), the incident particle cannot interact more than once with a given target nucleon and the target nucleons have no time for interactions with each other during the scattering process.

The next and very important assumption is that the nuclear potential V_A is built up from spatially separated potentials corresponding to nucleons. In this case the phase shift on the nucleus, $\chi_A(b)$, is equal to the sum of phase shifts $\chi_N(b_i)$ for each hadron-nucleon scattering:

$$\chi_A(b) = \sum_{i=1}^{A} \chi_N(b_i) \ . \tag{11.3}$$

The phases $\chi_A(b)$ and $\chi_N(b_i)$ are directly related to the elastic scattering amplitudes on the nucleus F^{el}_{hA} and on the isolated nucleon F^{el}_{hN}, respectively:

$$f^{el}(q) = \frac{ik}{2\pi} \int d^2b \, \Gamma(b) e^{iqb} \ , \tag{11.4}$$

$$\Gamma_N(b_j) = 1 - e^{i\chi_N(b_j)} \ , \tag{11.5}$$

$$\Gamma_A(b; r_1, ..., r_A) = 1 - e^{i\chi_A(b; r_1, ..., r_A)} = 1 - e^{i \sum_{j=1}^{A} \chi_j(b - b_j)} \ , \tag{11.6}$$

where $r_1, ..., r_A$ are the positions of the nucleons and b_j are their transverse coordinates. Only $A-1$ of the nucleon coordinates are independent, because $\Sigma_{j=1}^{A} r_j = 0$; this leads to the so-called center-of-mass motion correction.

Let us note that the amplitudes F^{el} differ from the amplitudes f^{el} unly by the fact that the first ones are defined in laboratory system. The optical theorem for F^{el} reads:

$$ImF^{el}(s, 0) = \frac{k}{4\pi} \sigma^{tot} \ . \tag{11.7}$$

11.2 Elastic scattering on a deuteron target

Let r_p and r_n be the coordinates of the proton and the neutron, $\vec{r} = \vec{r}_p - \vec{r}_n$, $b_1/2$ and $-b_1/2$ their transverse coordinates. The elastic scattering hd amplitude can be written in Glauber theory as

$$F_{hd}^{el}(q) = \frac{ik}{2\pi} \int e^{iqb} d^2b \int \psi_f^*(r) \times \tag{11.8}$$
$$\times \left\{1 - e^{[i\chi_p(b+b_1/2)+i\chi_n(b-b_1/2)]}\right\} \psi_i(r) d^3r \ .$$

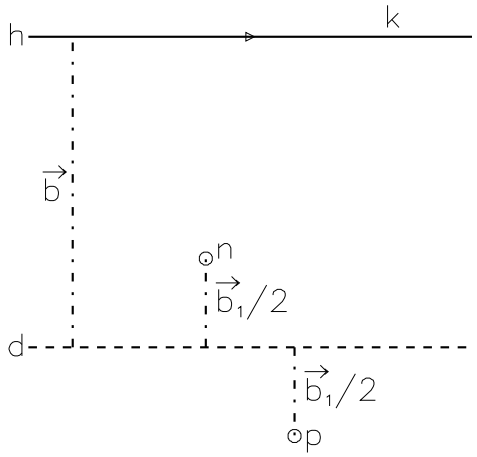

Figure 40: Elastic scattering of a fast hadron with momentum k on a deuteron target. All space vectors are two-dimensional.

After substituting f_{hN}^{el} ($\equiv f_p$ or f_n) instead of Γ_N, we obtain

$$\begin{aligned} F_{hd}^{el} &= \langle f|e^{iqb_1/2}F_p(q) + e^{-iqb_1/2}F_n(q) \qquad (11.9)\\ &+ \frac{i}{2\pi k}\int d^2q' e^{ib_1q'}F_p(q'+q/2)F_n(q'-q/2)|i\rangle \\ &= G_d(q/2)F_p(q) + G_d(q/2)F_n(q) \\ &+ \frac{i}{2\pi k}\int G_d(q')F_p(q/2-q')F_n(q/2+q')d^2q' \ , \end{aligned}$$

where

$$G_d(q) = \int e^{iqr}|\psi(r)|^2 d^3r \qquad (11.10)$$

is the deuteron form factor. It follows from the optical theorem that

$$\sigma_{hd}^{tot} = \sigma_{hp}^{tot} + \sigma_{hn}^{tot} - \Delta_2 \qquad (11.11)$$

with

$$\Delta_2 = \frac{2}{k^2}\int S_d(q)\,\mathrm{Im}f_p(q)\,\mathrm{Im}f_n(q)[1-\rho_p(q)\rho_n(q)]d^2q \ . \qquad (11.12)$$

Here Δ_2 is the Glauber correction for double scattering and

$$\rho_N(q) = \frac{Ref_N(q)}{Imf_N(q)} \ . \qquad (11.13)$$

11.3 Elastic scatterings on heavy nuclei

Let us now consider the elastic hA scattering, with the transition of the ground state A of the target nucleus to itself,

$$F_{hA}^{el}(q) = \frac{ik}{2\pi} \int d^2b e^{iqb} \langle A|\Gamma_A(b; r_1, ...r_A)|A\rangle \quad (11.14)$$

Using the expression for Γ_A and Γ_N Eq. (11.5) and the basic assumption Eq. (11.3), and carrying out a final transition from the phase back to the amplitudes, we obtain

$$\begin{aligned} F_{hA}^{el}(q) &= \frac{ik}{2\pi} \int d^2b e^{iqb} \int d^3r_1 ... d^3r_A \rho(r_1, ..., r_A) \quad (11.15) \\ &\times \prod_{i=1}^{A} \left[1 - \frac{1}{2\pi ik} \int d^2q_1 e^{-iq_1(b-b_i)} F_{hN}(q_1) \right] . \end{aligned}$$

Here b_i is the transverse coordinate of the ith nucleon, and $\rho(r_1, ..., r_A)$ is the probability distribution to find the nucleons in positions r_i.

One can reduce $\rho(r_1, ..., r_A)$ to the product of one-particle densities $\rho(r_i)$

$$\rho(r_1, ..., r_A) = \prod_{i=1}^{A} \rho(r_i) \ , \int d^3r_i \rho(r_i) = 1 \ . \quad (11.16)$$

After integrating over the positions of the nucleons we get

$$F_{hA}^{el}(q) = \frac{ik}{2\pi} \int d^2b e^{iqb} \left[1 - \left(1 - \frac{1}{2\pi ik} \int d^2q_1 e^{-iq_1 b} F_{hN}(q_1) G(q \right. \right. \tag{11.17}$$

where

$$G(q_1) = \int d^3r_i \rho(r_i) e^{iq_1 r_i} \tag{11.18}$$

is the one-particle nucleus form factor.

For further simplification for purely imaginary $ReF_{hN}(q \simeq 0)/ImF_{hN}(q \simeq 0) \ll 1$. F_{hN} and $A \gg 1$ the optical theorem gives

$$F_{hA}^{el}(q) = \frac{ik}{2\pi} \int d^2b e^{iqb} \left[1 - e^{-1/2\sigma T(b)} \right] \ , \sigma = \sigma_{hN}^{tot} \ . \tag{11.19}$$

In particular,

$$\sigma_{hA}^{tot} = 2 \int d^2b \left[1 - e^{-(1/2)\sigma T(b)} \right] \ , \tag{11.20}$$

$$\sigma_{hA}^{el} = \int d^2b \left[1 - e^{-(1/2)\sigma T(b)} \right]^2 \tag{11.21}$$

and

$$\sigma_{hA}^{inel} = \int d^2b \left[1 - e^{-\sigma T(b)} \right] \ . \tag{11.22}$$

11.4 Experimental proton and neutron distributions in the nuclei

Contrary to the case of eA scattering, hadron-nucleus collisions give information about the distribution not of the nuclear charge, but of nuclear matter.

Comparing the eA and hA experimental data, one can obtain separated distributions of protons and neutrons in nuclei. The question about the expected difference of proton and neutron distributions in heavy nuclei is not so simple. From one point of view the additional neutrons should increase the absolute values of their distributions in the whole nuclear volume.

Experimentally the case of proton-nucleus scattering; a lot of experimental data exists here. Some examples for the data and their theoretical description are shown in Fig. 44.

The distributions of protons were taken from electron scattering data, the neutron parameters were found by fitting theoretical cross sections to the experimental pA data. In addition to the Woods–Saxon

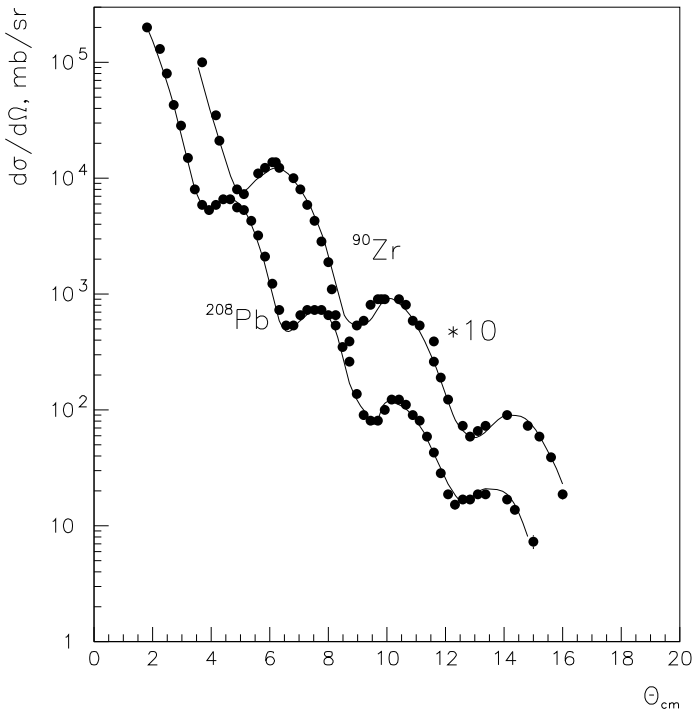

Figure 41: Differential cross sections for 1 GeV proton scattering on ^{90}Zr and ^{208}Pb nuclei together with their description by Glauber theory.

nuclear distribution, the more complicate form

$$\tilde{\rho}(r) = \rho_0 \frac{1 + w(r/c)^2}{1 + e^{(r-c)/a}} \qquad (11.23)$$

was also used.

The main result is that the difference in the radii of proton and neutron distributions is very small. In Table 8 we present several examples.

Nucleus	r_p	r_n	$r_n - r_p$
^{32}S	3.24	3.24	0.00
^{40}Ca	3.48	3.50	0.02
^{48}Ca	3.47	3.66	0.19
^{48}Ti	3.58	3.68	0.10
^{58}Ni	3.76	3.72	-0.04
^{64}Ni	3.84	3.83	-0.01
^{90}Zr	4.26	4.37	0.11
^{208}Pb	5.50	5.50	0.00

Table 8
Parameters of the proton and neutron folded densities, r_p and r_n are r.m.s. radii (in fm) of proton and neutron distributions respectively.

One can see that the difference in the r.m.s. radii $r_n - r_p$ is rather small, with the only exceptions of the cases ^{40}Ca and ^{48}Ca, where the difference is in eight additional neutrons, and in the case of ^{90}Zr.

12 Possibilities of Practical Use of High Energy Physics

12.1 Geological survey and investigation of the Earth structure with the help of neutrino beams

Low ebergy neutrino has very small interaction cross section, so it can cross the Earth without interaction. This cross section increase linearly with the initial energy E_ν. In lab. system

$$\sigma(\nu N)/E_\nu \sim 10^{-11}\text{mb/GeV} \ , \qquad (12.1)$$

and the energies of the order of hundreds GeV obey the significant probability of interactions on the lengh of penetration of several thousands km inside the Earth. Muon neutrinos are produced by an accelerator (block A in Fig. 45 via the decay of secondary charged pions $\pi \to \mu + \nu_\mu$ produced on any target.

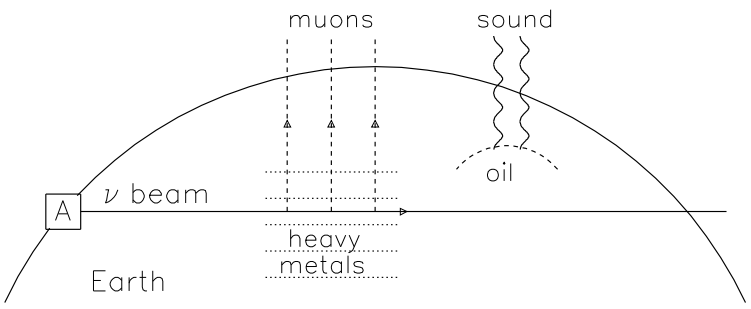

Figure 42: General scheme of geological survey of the Earth.

In the case of heavy metal (copper, silver, gold, lead, etc.) ore on the neutrino beam trajectory one can see an increase of muon production from the charged current reaction $\nu_\mu + N \to \mu^- + X$ because the average density of such ores are significantly larger that the average density of the Earth's crust. In the case of undergraund oil-field a specific acustic signal can be registrated, etc.

In the case of neutrino beam trajectory near to vertical direction one can investigate the general structure of the Earth including its kernel, etc.

12.2 Muon catalyzed fusion and nuclear energy production.

The reaction of nuclear fusion of heavy hydrogen isotopes, deuteron d and tritium t

$$d + t \rightarrow^4 \mathrm{He} + n + 17.6\mathrm{MeV} \qquad (12.2)$$

usually needs a high temperatures due to the Coulomb repalsion between d and t. This repulsion begins when the distance between d and t becomes smaller that the range of the correspondent atom D and T. The atomic radii are proportional to the inverse value of the mass of electron, m_e. So it is clear that if one can change an electron by a negative muon which is 200 times more heavy ($m_\mu/m_e \sim 200$), the role of repulsion significantly decrease. The estimations which are confirmed by the experimental data show that the reaction

$$d + t_\mu \rightarrow^4 \mathrm{He} + n + \mu^- + 17.6\mathrm{MeV} \qquad (12.3)$$

can occur at normal temperatures and densities. Very important point is that the final muon in the reaction Eq. (11.3) stay free with probability more than 99% (its state overlap very weakly with the wave functions of $^4\mathrm{He}_\mu$ atom in the momentum representation).

After that this muon can induce next fusion reaction, etc., so we can consider this muon as the catalizator of the process of Eq. (12.3). The muon mean life time is many times larger than the time of this processes.

The neutrons obtained in the process of Eq. (12.3) can be used directly as high intensity monoenergetical neutron source, say, for material science, or for the production a fuel for via reaction $n+^{238}\mathrm{U} \rightarrow ^{239}\mathrm{Pu} + \mathrm{X}$.

The general scheme of 14.1 MeV neutrons production via muon catalyzed fusion is presented in Fig. 46.

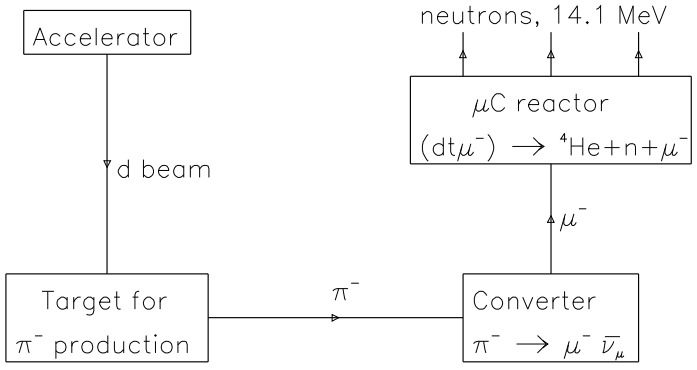

Figure 43: General scheme of high intensity 14.1 MeV neutrons production via muon catalyzed fusion.

Firstly we use, say, deuteron beam from accelerator with kinetic energy about 1 GeV per nucleon. for the production π^- on the target. Deuteron beam is preferable because negative pions are produced mainly in reactions with neutrons, see Exercises 1 and 2. The kinetic energy about 1 GeV per nucleon is near to the optimal value. At lower energies the pion production cross section becomes too small in comparison with elastic and quasielastic cross section, at higher energies the number of π^- produced by the unit of energy decreases.

The produced negative pions decay into muons in the converter, where the special configuration of magnetic fields optimize the losses of muons.

After that μ^- turn to μ-catalize reactor with mixture of deuterium and tritium where the 14.1 MeV neutrons are produced in the reaction Eq. (12.3). These neutrons can be used for the experiments or used for production of ^{2}39Pu from ^{2}38U for the futher use of this plutonium in usual nuclear plants for the electrical energy production.

12.3 Proton terapy

Sometimes people have serious medical problems, for example swelling, aneurisma, etc. and the standard surgical methods can not be used, for example the problem is inside brains. In this case the beam of high energy particles, usually protons can be used as it is schematically shown in Fig. 47.

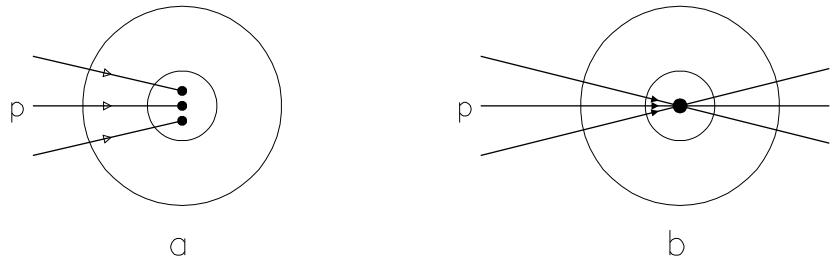

Figure 44: General scheme of use high energy particle beam in medicine. A part of body is shown by dashed circle and an affected region by solid circle.

there exist two possibilities, the energy can be taken by such a way that the beam will be stopped inside the affected region, see Fig. 50a or beam can penetrate all the body using different trajectories but everytime with the crossing point inside the affected region, see

Fig. 50b. Both methods have some preferencies and problems and both are used with very successful results.

13 Exercises

To SEction 2

Exercise 1:

Calculate the ratio of π^+ to π^0 production using the diagrams in Fig. 2 and the table of Clebsch-Gordan coefficients. Proton and neutron have isospin 1/2 with projections +1/2 and -1/2, π^+ and π^0 have isospin 1 with projections +1 and 0, and Δ^{++} and Δ^+ have isospin 3/2 with projections +3/2 and +1/2, respectively.

Exercise 2:

Calculate the ratio of π^+ to π^0 and to π^- production in proton-neutron collisions using similar diagrams to those Fig. 2 and the table of Clebsch-Gordan coefficients.

Exercise 3:

Using the results of above exercises, isospine invariance, the and table of Clebsch-Gordan coefficients, calculate the ratio of π^+ production cross sections in

pp and pn collisions.

To Section 3

Execise 4

Prove Eqs. (3.5), (3.8), and (3.9).

Execise 5

If s-channel reaction is $\pi^- p \rightarrow \pi^0 n$, what are t-channels and u-channels reactions ?

Exercise 6

Prove Eq. (7.23).

Exercise 7

Prove Eqs. (8.5).

Exercise 8

Obtain Glauber cross section for p^3H scattering

14 Specific Bibliography

1. Nuclear and Particle Physics, by W.E. Burcham and M. Jobes, Harlow, Essex: Longman Scientific and Technical, cop. 1995.

2. An Introduction to Regge Theory and High Energy Physics, by P.D.B. Collins, Cambridge University Press, 1977.

3. Quark Model and High Energy Collisions, by V.V. Anisovich, M.N. Kobrinsky, J. Nyri, and Yu.M. Shabelski, World Scientific, 2004.

4. Regge Poles in Particle Physics, by P.D.B. Collins and E.J. Squires, Springer Tracts in Modern Physics, volume 45, Springer-Verlag, 1968.

5. Review of Particle Physics, by S. Eidelman et al., Phys. Lett. **B**592, 2004.

6. Regge Poles in QCD, by A.B. Kaidalov, arXiv:hep-ph/0103011.

7. Models of High Energy Processes, by J.C. Polkinghorne, Cambridge University Press.

8. Regge Theory and High Energy Hadron-Nucleus

Scattering, by J.H. Weiss, Ref. TH. 2197-CERN.

9. Efectos Sombra Anómalos en las Colisiones Hadrón-Núcleo y Núcleo-Núcleo (Ph.D. Thesis), by A. Vázquez Ramallo (advisor Carlos Pajares Vales, USC, 1982.

10. El Modelo Dual de Partones y la Búsqueda del Plasma de Quarks y Gluones (Ph.D. Thesis), by C. Merino (advisor Carlos Pajares Vales), USC, 1991.

11. V.B.Berestetsky, Em.M.Lifshitz, L.P.Pitaevsky. Relativistic Quantum Theory. Part 1 Preferably after 1989.

12. L.B. Okun Weak Interactions of Elementary Particles.

(and references therein).